

Theoretical studies of electronic transport in monolayer and bilayer phosphorene: A critical overview

Gautam Gaddemane,¹ William G. Vandenberghe,¹ Maarten L. Van de Put,¹ Shanmeng Chen,¹
Sabyasachi Tiwari,¹ Edward Chen,² and Massimo V. Fischetti¹

¹Department of Materials Science and Engineering, The University of Texas at Dallas, 800 W. Campbell Rd., Richardson, Texas 75080, USA

²Corporate Research, Taiwan Semiconductor Manufacturing Company Ltd. 168, Park Ave. II,
Hsinchu Science Park, Hsinchu 300-75, Taiwan, Republic of China



(Received 30 January 2018; revised manuscript received 12 July 2018; published 7 September 2018)

Recent *ab initio* theoretical calculations of the electrical performance of several two-dimensional materials predict a low-field carrier mobility that spans several orders of magnitude (from 26 000 to 35 cm² V⁻¹ s⁻¹, for example, for the hole mobility in monolayer phosphorene) depending on the physical approximations used. Given this state of uncertainty, we review critically the physical models employed, considering phosphorene, a group-V material, as a specific example. We argue that the use of the most accurate models results in a calculated performance that is at the disappointing lower end of the predicted range. We also employ first-principles methods to study high-field transport characteristics in monolayer and bilayer phosphorene. For thin multilayer phosphorene we confirm the most disappointing results, with a strongly anisotropic carrier mobility that does not exceed ~ 30 cm² V⁻¹ s⁻¹ at 300 K for electrons along the armchair direction. We also discuss the dependence of low-field carrier mobility on the thickness of multilayer phosphorene.

DOI: [10.1103/PhysRevB.98.115416](https://doi.org/10.1103/PhysRevB.98.115416)

I. INTRODUCTION

In the past couple of decades, the theoretical study of electronic transport in semiconductors has been affected by two new driving factors. First, the effort to scale transistors to the nanometer size has stimulated interest in materials and devices that are quite different from the “conventional” materials employed by the microelectronics industry. References [1–3] constitute excellent recent overviews of the state of the art. Unlike silicon, germanium, or III-V compound semiconductors, for which decades of study have resulted in a reliable database of their electronic properties (e.g., band gap, effective mass, and carrier mobility), the atomic, electronic, and transport properties of many of these new materials are, at best, poorly known; at worst, even their existence and stability are known only from theoretical predictions. The infancy of the technology used to deal with these materials also casts doubts on the usefulness of experimental results because of the large deviations from ideality that are expected from such an immature and fast-changing technology.

The second driving cause is the timely and welcome progress recently made in *ab initio* (or “first-principles”) theoretical methods. Whereas in the past their predictions have been limited to small systems and had little or no connection to electronic transport, recent progress made in physical understanding, numerical algorithms, and computing hardware has broadened their range of applications, improved their accuracy, and extended their scope to electronic transport [4]. Density functional theory (DFT) is now routinely used to predict the atomic and electronic structure of these new materials, thanks to the wide availability of computer

packages, such as the Vienna *ab initio* software package (VASP) [5–8] or QUANTUM ESPRESSO (QE) [9]. Even the strength of the electron-phonon interaction can now be calculated using DFT by using either finite ion displacements [10] or density functional perturbation theory (DFPT) [11,12], a remarkable evolution since the early “pioneering” days in which the rigid-ion approximation [13] and empirical pseudopotentials were painstakingly used to estimate deformation potentials in Si, intervalley deformation potentials in III-V compound semiconductors [14,15], and used in Monte Carlo transport studies [16,17]. Even transport in open systems has been studied using DFT [18] and such an *ab initio* formalism has also been used to study dissipative transport in the two-dimensional materials of current interest [19].

Despite this remarkable progress, and limiting ourselves to the carrier mobility in covalent two-dimensional materials, theoretical predictions reported in the literature disagree wildly. Our purpose here is to analyze critically the situation we face regarding phosphorene, taken as a striking example of this uncertainty and disagreement that is due to both physical and computational aspects, understand the underlying causes, learn from this how we should proceed, and consider in detail low-field and high-field electronic transport in phosphorene. Therefore, this paper is organized as follows: In Sec. II we discuss the state of the art regarding the carrier mobility in phosphorene, presenting results obtained in a simplified but realistic model for monolayer phosphorene. In Sec. III we present a general theoretical framework to study low- and high-field electronic transport in two-dimensional (2D) crystals using DFT. Finally, we present our results for monolayer and bilayer phosphorene in Sec. IV.

II. CARRIER MOBILITY IN PHOSPHORENE

Monolayer or few-layer black phosphorus (bP), or phosphorene, is one of the many two-dimensional materials that have attracted enormous interest since the isolation of graphene [20]. Considering only covalent crystals, notable examples that we shall mention or consider explicitly here include silicene [21–24], germanene [25,26], phosphorene itself, of course [27–35], arsenene [36–39], antimonene [38–41], stanene [42–44], and another large-band-gap two-dimensional topological insulator, bismuthene [45,46] which, known since the 1990's, has become the subject of recent renewed interest [47,48]. Interest in phosphorene presumably originates from the very large carrier mobility measured in bulk black phosphorous [49,50]. This interest has been reinforced by the good measured electrical properties of field-effect transistors (FETs) having many-layer phosphorene as channel material [28–35]. Despite such wide interest, to our knowledge, the intrinsic charge-transport characteristics of monolayer phosphorene have not been widely studied experimentally, having been reported only in Ref. [31]. Moreover, theoretical predictions are in wild disagreement. We shall now review the experimental and theoretical information available at present, before discussing the causes of the theoretical confusion.

A. Available experimental and theoretical results

Given the large number of studies that have been published regarding the carrier mobility in phosphorene, it is convenient to summarize in Tables I and II the available experimental and theoretical results, before commenting on them. A necessary critical review will follow, as anticipated.

Experimental information. As we have mentioned above, interest in phosphorene has been stimulated by the relatively high room-temperature carrier mobility measured in black phosphorus: 300 to 1100 $\text{cm}^2 \text{V}^{-1} \text{s}^{-1}$ for electrons and 150 to 1300 $\text{cm}^2 \text{V}^{-1} \text{s}^{-1}$ for holes, depending on orientation [49]. Information for multilayers is limited to the hole mobility since samples are almost invariably *p* type. Only Cao *et al.* [31] have observed ambipolar behavior in field-effect transistors with monolayer, bilayer, and trilayer channels, finding an electron mobility much smaller than the hole mobility

TABLE I. Experimentally measured hole mobility μ_h in phosphorene multilayers at 300 K.

| Reference | μ_h ($\text{cm}^2 \text{V}^{-1} \text{s}^{-1}$) | Thickness |
|-----------------------------|---|-----------------------|
| Akahama <i>et al.</i> [49] | 150–1300 | Bulk black phosphorus |
| Li <i>et al.</i> [29] | 300–1000 | >10 nm |
| Xia <i>et al.</i> [28] | 600 | 15 nm |
| Gillgren <i>et al.</i> [34] | 400 | “Few layers” |
| Doganov <i>et al.</i> [32] | 189 | 10 nm |
| Xia <i>et al.</i> [28] | 400 | 8 nm |
| Liu <i>et al.</i> [30] | 286 | 5 nm |
| Xiang <i>et al.</i> [33] | 214 | 4.8 nm |
| Cao <i>et al.</i> [31] | 1 | Monolayers |
| Cao <i>et al.</i> [31] | 80 | Bilayers |
| Cao <i>et al.</i> [31] | 1200 | Trilayers |

TABLE II. Theoretical calculations of the 300-K electron and hole mobility μ_e and μ_h in monolayer and bilayer phosphorene.

| Reference | μ_e ($\text{cm}^2 \text{V}^{-1} \text{s}^{-1}$) | | μ_h ($\text{cm}^2 \text{V}^{-1} \text{s}^{-1}$) | |
|-------------------------------------|---|---------|---|---------------|
| | Armchair | Zigzag | Armchair | Zigzag |
| Monolayers | | | | |
| Qiao <i>et al.</i> ^a | 1100 | 80 | 640–700 | 10 000–26 000 |
| Jin <i>et al.</i> ^b | 210 | 40 | 460 | 90 |
| Rudenko <i>et al.</i> ^c | 738 | 114 | 292 | 157 |
| Rudenko <i>et al.</i> ^d | ~700 | | ~250 | |
| Trushkov <i>et al.</i> ^e | 625 | 82 | | |
| Liao <i>et al.</i> ^f | 170 | 50 | 170 | 35 |
| This work ^g | 20 | 10 | 19 | 2.4 |
| This work ^h | 21 | 10 | 19 | 3 |
| This work ⁱ | 25 | 5 | | |
| Bilayers | | | | |
| Qiao <i>et al.</i> ^a | 600 | 140–160 | 2600–2800 | 1300–2200 |
| Jin <i>et al.</i> ^b | 1,020 | 360 | 1,610 | 760 |
| This work ^g | 14 | 7 | 12 | 2 |
| This work ^h | 24 | 4 | 15 | 3 |
| This work ^j | 50 | 19 | 34 | 13 |

^aReference [51].

^bReference [52], Monte Carlo and DFT (DFPT).

^cReference [54], LA and TA, one-phonon processes.

^dReference [54], LA and TA, one- and two-phonon processes.

^eReference [53], LA and TA, at a density of 10^{13} electrons/ cm^2 .

^fReference [55], DFT (DFPT).

^gMonte Carlo and DFT (finite differences), acoustic and optical phonons.

^hMonte Carlo and DFT (DFPT).

ⁱKubo–Greenwood, acoustic phonons only, elastic and equipartition approximation.

^jMonte Carlo and DFT (DFPT), absence of low-energy optical modes.

in all cases. They have also provided the only measurement for charge-transport properties of monolayers. In all cases, the hole mobility is strongly anisotropic and shows a strong dependence on the thickness of the film. Specifically, Cao *et al.* [31] have measured a room-temperature hole mobility of 1, 80, and 1200 $\text{cm}^2 \text{V}^{-1} \text{s}^{-1}$ in monolayers, bilayers, and trilayers. Li *et al.* [29] have also observed a thickness dependence, reporting a 300-K hole mobility of around several hundred $\text{cm}^2 \text{V}^{-1} \text{s}^{-1}$ for thick layers, sharply decreasing in layers thinner than 10 nm, and reaching values as low as 1–10 $\text{cm}^2 \text{V}^{-1} \text{s}^{-1}$ for layers 2–3 nm thin [29]. A similar trend has been reported also by Liu *et al.* [30], with a peak field-effect hole mobility of 286 $\text{cm}^2 \text{V}^{-1} \text{s}^{-1}$ in 5-nm-thick films. Xia *et al.* [28] found a Hall mobility of about 600 $\text{cm}^2 \text{V}^{-1} \text{s}^{-1}$ in 15-nm-thick films and of about 400 $\text{cm}^2 \text{V}^{-1} \text{s}^{-1}$ in 8-nm-thick films. The general trend of an increasing mobility in thicker films is also confirmed by the results of Xiang *et al.* [33], who have measured a hole mobility of 214 $\text{cm}^2 \text{V}^{-1} \text{s}^{-1}$ in 4.8-nm-thick films, compared to a Hall mobility of 400 $\text{cm}^2 \text{V}^{-1} \text{s}^{-1}$ observed in “few-layers” phosphorene by Gillgren *et al.* [34]. As a rare example of information on electron transport, Doganov and co-workers [32] have reported an electron mobility of about 106 $\text{cm}^2 \text{V}^{-1} \text{s}^{-1}$ in 10-nm-thick films. For holes, they have measured a value of

$189 \text{ cm}^2 \text{ V}^{-1} \text{ s}^{-1}$. Note that these are field-effect mobilities. Finally, a similar thickness dependence has been observed also at low temperatures by Tayari and co-workers [35], who have considered black-phosphorus films with thickness in the range of 6.1–47 nm and have measured a maximum mobility of about 600 (below 80 K) and 900 (300 mK) $\text{cm}^2 \text{ V}^{-1} \text{ s}^{-1}$ in their thickest films. In most of these experiments, the highest field-effect hole mobility has been measured for channels presumably oriented along the armchair direction (“presumably” only, since this information is not always given).

Theoretical results. Restricting again our attention to room-temperature data, in monolayers a relatively large hole mobility of about $640\text{--}700 \text{ cm}^2 \text{ V}^{-1} \text{ s}^{-1}$ has been calculated by Qiao and co-workers for transport along the armchair direction [51]. Surprisingly, a huge hole mobility $10\,000\text{--}26\,000 \text{ cm}^2 \text{ V}^{-1} \text{ s}^{-1}$ has been predicted along the heavy-mass zigzag direction [51], a result allegedly due to an extremely small deformation potential. For electrons, Qiao *et al.* [51] have calculated a mobility of 1100 (armchair) and 80 (zigzag) $\text{cm}^2 \text{ V}^{-1} \text{ s}^{-1}$. Monte Carlo simulations based on the DFT-calculated band structure and carrier-phonon scattering rates [9] have been performed by Jin *et al.* [52]. They have obtained a hole mobility of 460 and $90 \text{ cm}^2 \text{ V}^{-1} \text{ s}^{-1}$ for transport along the armchair and zigzag directions, respectively. For electrons, these values are, instead, 210 (armchair) and 40 (zigzag) $\text{cm}^2 \text{ V}^{-1} \text{ s}^{-1}$. They have also predicted a higher mobility in bilayers: $1020 \text{ cm}^2 \text{ V}^{-1} \text{ s}^{-1}$ (armchair) and $360 \text{ cm}^2 \text{ V}^{-1} \text{ s}^{-1}$ (zigzag) at 300 K for electrons, $1610 \text{ cm}^2 \text{ V}^{-1} \text{ s}^{-1}$ (armchair) and $760 \text{ cm}^2 \text{ V}^{-1} \text{ s}^{-1}$ (zigzag) for holes. This enhanced mobility has been attributed to the smaller hole effective mass in bilayers, especially along the “flat” Γ -Y (zigzag) direction, as indicated by Qiao *et al.* [51]. We shall later discuss (or, better, speculate about) possible causes for the observed thickness dependence of the hole mobility. More recently, Trushkov and Perebeinos [53] have calculated the electron mobility as a function of carrier density and temperature, obtaining values of $625 \text{ cm}^2 \text{ V}^{-1} \text{ s}^{-1}$ (armchair) and $82 \text{ cm}^2 \text{ V}^{-1} \text{ s}^{-1}$ (zigzag) at 300 K and at an electron density of 10^{13} cm^{-2} . Rudenko and co-workers [54] have obtained similar values of 738 (armchair) and 114 (zigzag) $\text{cm}^2 \text{ V}^{-1} \text{ s}^{-1}$ for electrons, of 292 (armchair) and 157 (zigzag) $\text{cm}^2 \text{ V}^{-1} \text{ s}^{-1}$ for holes. At the lower range of predicted mobility, Liao *et al.* [55] have also used DFT to calculate the band structure and carrier-phonon matrix elements, obtaining the values of 170 (armchair) and 50 (zigzag) $\text{cm}^2 \text{ V}^{-1} \text{ s}^{-1}$ for electrons, and 170 (armchair) and 35 (zigzag) $\text{cm}^2 \text{ V}^{-1} \text{ s}^{-1}$ for holes.

B. Why such a disagreement?

It is probably premature to compare the experimental and theoretical results summarized in Tables I and II. Indeed, different experimental results may be due to expected deviations from ideality of the material, such as impurities and defects, resulting from an immature technology. Moreover, experimental data have been obtained in supported, and often gated, layers, whereas theoretical calculations have considered ideal free-standing films. A proper discussion of this issue would distract us from the main focus of this paper. Here, we shall only remark that changes of the phonon spectra may be expected when moving from free-standing

layers to supported and gated materials. This, obviously and in principle, may affect the carrier mobility. For van der Waals materials such as graphene, in-plane acoustic modes are left largely unaffected by interactions with a substrate, even when as strong as coupling with metals, whereas optical phonons are slightly softened by the dielectric screening of the metal [56]. An excellent review of phonon dynamics in 2D materials also highlights the 2D nature of the layer(s) as the major effect that controls the vibrational frequencies [57]. Moreover, as we have already remarked, most calculations have been performed assuming intrinsic materials, whereas experiments usually deal with gated layers at a high carrier density. Given this “circumstantial” evidence, and ignoring scattering with nonidealities of the substrate/gate (charges and defects), coupling with hybrid plasmon/substrate-optical modes [58], and considering that acoustic flexural modes, indeed affected by the substrate and the gate, do not play any role in phosphorene, we should not expect gross changes of the electronic-transport properties, at least in van der Waals materials. However, as discussed below, phosphorene is not a pure “van der Waals” material. Therefore, it may couple rather strongly with a substrate or gate insulator. Depending on the vibrational stiffness (e.g., SiO_2) or softness (e.g., HfO_2) of this layer, the spectrum of the acoustic and especially of the optical modes of phosphorene will be affected accordingly. Nevertheless, here we wish to focus on the wide variations of the theoretical predictions for free-standing layers listed in Table II.

Indeed, aside from an obvious thickness and orientation dependence, we have already observed that the wide variations of the experimental data shown in Table I may be explained by deviations from ideality of the material. No such plausible explanation can easily be found to make sense of the surprisingly wide range of theoretically predicted values shown in Table II. This is a disconcerting observation since most of the theoretical results have been obtained by using first-principles calculations (DFT), often from the same software packages.

Obviously, even *ab initio* DFT calculations, despite their elegance and predictive power, exhibit some limitations. For example, the behavior of the electronic dispersion near the top of the valence band in monolayer and multilayer phosphorene is very flat. The details of this dispersion (that is, effective mass and velocity) depend strongly on the exact details of the calculation [59,60], so much so that a hole effective mass along the zigzag direction cannot be defined. Such details may matter only marginally when considering the overall band structure, but the equilibrium transport properties are strongly affected by such tiny differences, being extremely sensitive to variations of the order of the thermal energy. These variations affect the carrier velocity and the density of states that, in turn, affects the scattering rates. Moreover, the carrier-phonon matrix elements obtained from DFT calculations may suffer from errors and uncertainties related not only to the choice of pseudopotentials and exchange-correlation functionals, but also to the subtle issue of dielectric screening. This has been observed to be the case for graphene [61–63], resulting in underestimated deformation potentials [64], as discussed in Ref. [65]. Therefore, different choices of pseudopotentials or exchange-correlation functionals [local density approximation (LDA), generalized gradient approximation (GGA), or

hybrid exchange-correlation functionals], or the use of GW corrections, will result in different band structures and values of the total energy, and so in different phonon spectra and electron-phonon matrix elements. However, it is difficult to see how such uncertainties, as large as they might be, may result in almost 4 orders of magnitude variations seen in Table II for the hole mobility along the zigzag directions, from 10 000–26 000 cm² V⁻¹ s⁻¹ (Ref. [51]) to the small values of the order unity that we shall present below.

In our opinion, an opinion that is also shared by Nakamura and co-workers [66], a first *major* source of errors is the use of the so-called Takagi formula [67] to calculate the carrier mobility for a two-dimensional electron gas (2DEG):

$$\mu = \frac{e\hbar^3 C_{2D}}{k_B T m^* m_d E_1^2}. \quad (1)$$

In this expression, m^* and m_d are the conductivity and density-of-states effective masses, respectively, C_{2D} is the longitudinal or transverse elastic constant of the 2D materials, and E_1 is the so-called “deformation potential.” In this context, this last all-important quantity is defined as the energy shift $\Delta E_{c,v}$ of the relevant band edge (conduction for electron transport, valence for holes), under a relative change $\Delta a/a_0$ of the lattice constant a_0 ,

$$E_1 = a_0 \frac{\Delta E_{c,v}}{\Delta a}. \quad (2)$$

Approximations equivalent to those implied by Eq. (1) have also been used to calculate extremely high values for the carrier mobility in silicene ($\approx 2 \times 10^5$ cm² V⁻¹ s⁻¹ for both electrons and holes) [68] and germanene ($\approx 6 \times 10^5$ cm² V⁻¹ s⁻¹ for both electrons and holes) [69], ignoring coupling to flexural acoustic modes [70]. Equation (1) must be used with extreme care. It was originally derived by Takagi *et al.* [67] in the context of electron transport in Si inversion layers. It was intended to be used to calculate the mobility limited by scattering with acoustic phonons, only one of the many scattering processes that affect electron transport in those systems, such as intersubband/intervalley process, scattering with optical phonons, with ionized impurities, and with surface roughness. Even when taken in this originally limited context, Eq. (1) is of a semiempirical nature since longitudinal and transverse acoustic phonons are lumped into one single “effective” mode, with an isotropic deformation potential E_1 , which for Si is typically in the range of 9–14 eV, fitted to reliably known experimental data. Indeed, within the framework of the deformation potential theorem [71], the electron/acoustic-phonon matrix elements in Si are known to be anisotropic [72], a property that plays a crucial role in explaining the electron mobility in strained Si (Ref. [73]) and Si inversion layers [74]. Arbitrarily extending Eq. (1) to the more general context of 2D crystals presents severe problems: Scattering with optical modes and intervalley processes, when present, are neglected by Eq. (1). Moreover, as we have emphasized, only one phonon mode is considered, LA or TA, depending on the choice of E_1 and C_{2D} ; also neglected is the anisotropy of the deformation potential, an effect that, as we have already noted, is extremely important in Si (Refs. [72–74]) and that has also been shown to be equally important in phosphorene [55]. Finally, the symmetry of the initial and final wave functions

affects the magnitude and angular dependence of the carrier-phonon matrix elements, and these “wave-function-overlap effects” are also ignored altogether. Therefore, the results of Qiao *et al.* [51] should be regarded as no more than extremely optimistic upper bounds.

A second likely source of errors is the use of the “band deformation potential” (2) to approximate the electron-phonon matrix elements. Even when moving beyond Eq. (1) by using, for example, the Kubo-Greenwood expression to calculate the carrier mobility, the shifts of the band edges under various strain conditions give only a qualitative approximation for the scattering matrix elements since the effects mentioned above, mainly, wave-function overlap and angular dependence, are still neglected. Such models have been employed by Trushkov and Perebeinos [53] and by Rudenko and co-workers [54]. With a proper choice of elastic constants, the latter authors have accounted for both longitudinal acoustic (LA) and transverse acoustic (TA) phonons and for two-phonon processes between electrons and flexural modes. Yet, even in this case, their results, while not quite so impressive, are still quite large.

The fact that such models employing isotropic deformation potentials result in an optimistic overestimation of the mobility has been shown by the work performed by Dresselhaus’ group [55]. Accounting for all modes, for the anisotropy of the matrix elements (due mainly to wave-function-overlap effects) and accounting also for a nonparabolic band structure, they have predicted much smaller values. The results that we report here, listed in Table II, are even smaller. We shall speculate below on possible causes for such a disappointing disagreement.

In order to illustrate the importance of the anisotropy of the carrier-phonon matrix elements, we now present results for the electron mobility in monolayer phosphorene obtained using the Kubo-Greenwood method (see Supplemental Material for details [75]) in the simple case of scattering with acoustic modes, only using angular-dependent deformation potentials, parabolic bands, linear phonon dispersion, elastic and equipartition approximation. Figure 1 shows the acoustic deformation potentials for monolayer phosphorene plotted as a function of the final scattering angle. The anisotropy in the deformation potentials seen in this plot reinforces the importance of using angular-dependent deformation potentials over constant deformation potentials. The momentum relaxation rate and electron mobility are shown in Figs. 2 and 3. The results are sufficiently accurate to emphasize the importance of the effects ignored by Eqs. (1) and (2). Despite the relatively simple models we have used so far, the results are in excellent qualitative agreement, and even reasonable quantitative agreement, with our more accurate full-band Monte Carlo results presented in Sec. IV A below. Yet, both our results are significantly different from those reported in Refs. [52,55].

We can only speculate on possible physical and numerical causes of the difference between our results and those reported in Refs. [52,55]. In Ref. [55] the local density approximation (LDA) [76] is used for the exchange-correlation functional, as opposed to the Perdew-Burke-Ernzerhof generalized-gradient approximation (GGA-PBE) [77] we have used. However, regarding the effective masses, no information is available. Recently, Ponc e *et al.* [78] have shown for silicon that the

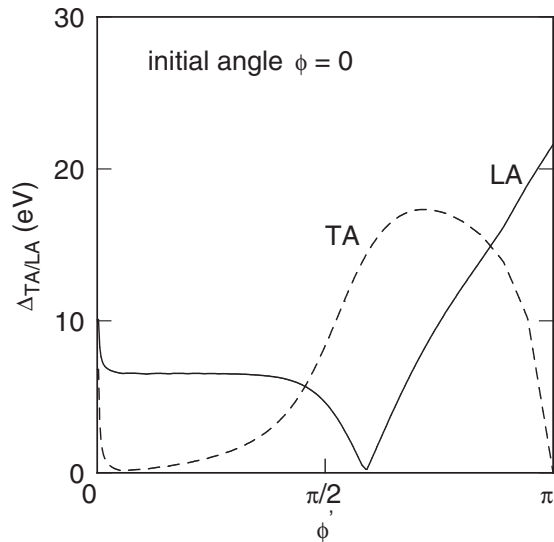


FIG. 1. Acoustic deformation potentials Δ_{LA} and Δ_{TA} as a function of the final scattering angle ϕ' (with respect to the armchair direction) for an initial angle $\phi = 0$, that is, for an initial \mathbf{k} state along the armchair direction.

effective masses are the most critical parameters to achieve predictive and accurate values of the mobility in silicon. In Table III we list the available effective masses, calculated from DFT. Even though Ref. [52] uses the GGA-PBE exchange-correlation functional, similar to ours, the effective masses obtained by them are quite different from ours and also from others who employed GGA-PBE (Table III). The above reasons might be the cause for the difference in both electronic and phononic structure, which may at least, in part, account for the observed difference. Indeed, as we shall emphasize below, great care must be taken, by using large supercells

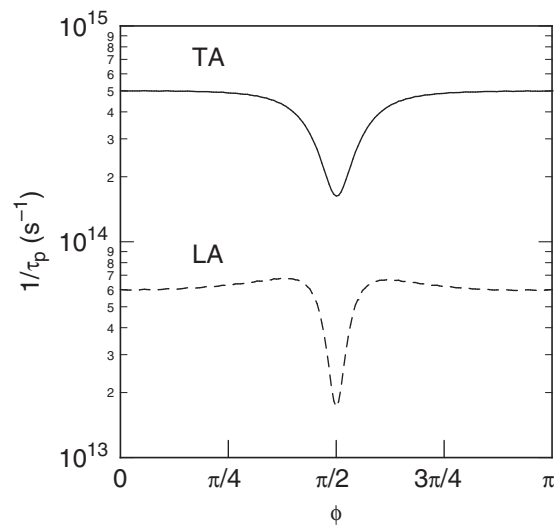


FIG. 2. Momentum relaxation rate for electron scattering with acoustic phonons, as a function of the angle ϕ between the \mathbf{k} vector and the armchair direction. Note that in the parabolic-band and elastic-equipartition approximations, the momentum relaxation rate does not depend on the electron kinetic energy.

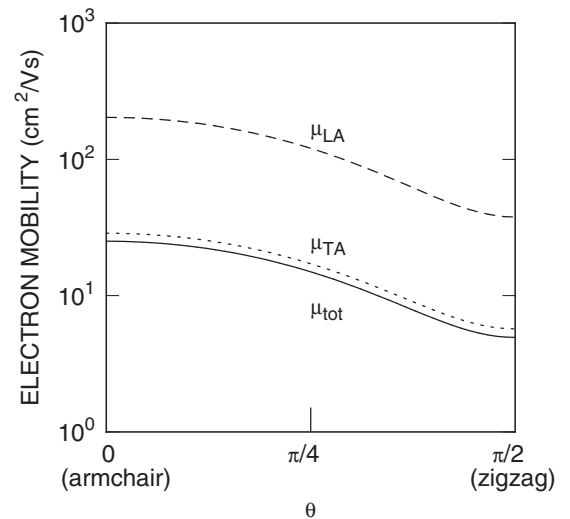


FIG. 3. Electron mobility in monolayer phosphorene at 300 K as a function of the angle θ between the transport direction and the armchair Γ - X symmetry line. The LA-phonon- and TA-phonon-limited mobilities are shown separately. These results have been obtained using the parabolic-band and elastic-equipartition approximations and ignoring scattering with optical phonons.

and strict thresholds for the phonon calculations, to avoid “negative” frequencies for the low-energy vibrational modes and, even when obtaining a “correct” vibrational spectrum, the resulting eigenvectors are only known with relatively small accuracy. Unfortunately, Refs. [52,55] do not provide any information regarding the phonon dispersion. Moreover, the calculation of the mobility requires numerical integrations over the Brillouin zone and we have found that a very fine discretization of the Brillouin zone is required to obtain accurate results. This is confirmed by Poncé *et al.* [78] who emphasize the importance of using extremely fine sampling of the momentum space for the scattering rates to calculate a fully

TABLE III. Calculated effective masses m_{Γ}^e and m_{Γ}^h in monolayer and bilayer phosphorene.

| Reference | m_{Γ}^e | | m_{Γ}^h | |
|-------------------------------------|----------------|--------|----------------|--------|
| | Armchair | Zigzag | Armchair | Zigzag |
| Monolayers | | | | |
| Qiao <i>et al.</i> ^a | 0.17 | 1.12 | 0.15 | 6.35 |
| Jin <i>et al.</i> ^b | 0.34 | 1.26 | 0.30 | 3.02 |
| Rudenko <i>et al.</i> ^c | 0.18 | 1.15 | 0.17 | 9 |
| Trushkov <i>et al.</i> ^d | 0.15 | 1.12 | | |
| This work ^e | 0.14 | 1.24 | 0.14 | N/A |
| Bilayers | | | | |
| Qiao <i>et al.</i> ^a | 0.18 | 1.13 | 0.15 | 1.81 |
| Jin <i>et al.</i> ^b | 0.41 | 1.35 | 0.33 | 4.76 |
| This work ^e | 0.10 | 1.33 | 0.09 | 3.08 |

^aReference [51], HSE06.

^bReference [52], PBE-GGA, ULTRASOFT.

^cReference [54], PBE-GGA, PAW.

^dReference [53], PBE-GGA.

^ePBE-GGA, PAW.

predictive carrier mobility. Specifically, as we shall see below, we have used a very fine mesh around the Γ -symmetry point, equivalent to 145×205 \mathbf{k} points in the first quadrant. On the contrary, a much coarser mesh, presumably 12×12 points in the entire BZ, has been employed in Ref. [52]. Despite the quantitative disagreement with the *ab initio* results presented in Refs. [52,55], we confirm their main conclusion: Aside from the obvious anisotropy of the conduction bands, these results show the importance of the additional matrix-element anisotropy. This effect explains the large values calculated by Qiao *et al.* [51] and also those reported in Refs. [53,54].

III. FIRST-PRINCIPLES PHYSICAL MODELS AND NUMERICAL METHODS

Having used a simplified model to draw some early conclusions, we now consider more accurate but less transparent *ab initio* methods.

A. Band structure and phonon spectrum

For the calculation of the band structure of the systems considered here, we have primarily used the Vienna *ab initio* simulation package (VASP) [5–8] with the Perdew-Burke-Enzerhoff generalized-gradient approximation (GGA-PBE) for the exchange-correlation functional [77] and a projector augmented wave (PAW) [79] pseudopotential. A vacuum “padding” of 20 Å was used in constructing the unit cell to obtain free-standing layers and avoid interaction with periodic images. Initially, we have always performed structural optimization by minimizing the total energy in order to determine the lattice constants and ionic positions. VASP also handles van der Waals (vdW) interactions, important in multilayer systems, with Grimme’s model [80]. We have chosen the “optPBE” functionals [81] among the various other vdW-corrected functionals [82,83] for the bilayers. We shall further discuss this issue below. The phonon spectra have been obtained using the PHONOPY computer program [84] which calculates the force constants using small-displacement method, using an interface to VASP to obtain the atomic forces. In our calculations, we have found that a supercell of size of at least $8 \times 8 \times 1$ unit cells is required to avoid unphysical imaginary frequencies for low-energy acoustic phonons, especially for the flexural out-of-plane (ZA) modes.

In light of the large discrepancies seen in literature when using different methods, we have decided to verify the results obtained from VASP using a different implementation of DFT, the QUANTUM ESPRESSO (QE) [9] package, so that we can independently calculate the atomic configuration and electronic structure for monolayer and bilayer phosphorene using ultrasoft pseudopotentials, and the PBE-GGA exchange-correlation approximation. The phonon spectra have been obtained by using QE, which yields the dynamical matrix using density functional perturbation theory (DFPT) [11], as opposed to the small-displacements method of PHONOPY. The phonon spectra obtained from QE are calculated on a coarse \mathbf{q} -points grid and interpolation to a fine grid, as required for the proper estimation of the scattering rates, is performed with minimal loss of accuracy by using maximally localized Wannier functions as implemented in the EPW [85,86] package.

In QE, the \mathbf{k} -point grid used in the self-consistent calculation of the electronic structure must be a multiple of the \mathbf{q} -point grid to obtain an accurate phonon dispersion. For both the VASP and QE methods, the self-consistent calculations should be performed using a large cutoff energy and strict thresholds to avoid negative frequencies, especially for the ZA phonons.

Recently, Sohler *et al.* [87] have discussed the necessity of avoiding artifacts arising from the long-range Coulomb interactions among adjacent supercells when dealing with the electronic structure, vibrational spectrum, and carrier-phonon interactions in 2D materials. This is a serious issue in charged layers (doped and/or gated) and in polar materials. However, in our case of charge-neutral nonpolar layers, we found that the use of a long-wavelength cutoff for the Hartree potential along the direction normal to the plane of the layer not only does not result in any significant difference in our calculations, but may also result in artifacts.

In any event, even though the methods differ significantly in their approach, both VASP and QE, with and without 2D screening, yield matching crystal structure, band structure, and phonon dispersion for both monolayer and bilayer phosphorene.

B. Carrier-phonon interaction

We have treated the electron-phonon interaction following the general theory developed in Refs. [10–12,64]. The matrix elements for the electron-phonon interaction can be expressed as

$$\begin{aligned} & \langle \mathbf{k}'n' | V_{\mathbf{q}}^{(\eta)} | \mathbf{k}n \rangle \\ &= \left\{ \frac{n_{\mathbf{q}}^{(\eta)1/2}}{(1+n_{\mathbf{q}}^{(\eta)})^{1/2}} \right\} \sum_{l,\gamma} \left(\frac{\hbar}{2N_c M_\gamma \omega_{\mathbf{q}}^{(\eta)}} \right)^{1/2} \\ & \quad \times e^{i\mathbf{q}\cdot\mathbf{R}_{l\gamma}} \widehat{\mathbf{e}}_{\mathbf{q},\gamma}^{(\eta)} \cdot \int_{\Omega} d\mathbf{r} \psi_{\mathbf{k}'n'}^*(\mathbf{r}) \frac{\partial U(\mathbf{r})}{\partial \mathbf{R}_{0,\gamma}} \psi_{\mathbf{k}n}(\mathbf{r}), \quad (3) \end{aligned}$$

where N_c is the number of cells, M_γ the mass of ion γ in each cell, Ω is the volume of the crystal, the index l labels the cells, $\mathbf{R}_{l\gamma}$ the equilibrium position of ion γ in cell l , \mathbf{k} , \mathbf{k}' and n , n' are the wave vectors and band indices of the initial and final electronic states, respectively, $\psi_{\mathbf{k}n}(\mathbf{r})$ are the associated Bloch wave functions, $\omega_{\mathbf{q}}^{(\eta)}$ is the phonon frequency, and $\widehat{\mathbf{e}}_{\mathbf{q},\gamma}^{(\eta)}$ the unit displacement vector of ion γ for a phonon of branch η and wave vector $\mathbf{q} = \mathbf{k}' - \mathbf{k}$. Here, \mathbf{r} , $\widehat{\mathbf{e}}_{\mathbf{q},\gamma}^{(\eta)}$, and $\mathbf{R}_{l\gamma}$ are three-dimensional (3D) vectors while \mathbf{k} , \mathbf{k}' , and \mathbf{q} are 2D vectors. The quantity $n_{\mathbf{q}}^{(\eta)}$ is the Bose-Einstein phonon occupation number (obtained after having implicitly traced out the phonon modes, assumed to be at equilibrium) for phonons of branch η and wave vector \mathbf{q} . The upper (lower) term within the curly brackets applies to phonon absorption (emission) processes. Finally, the term $\partial U(\mathbf{r})/\partial \mathbf{R}_{l,\gamma}$ represents the change of total energy of the lattice under a shift $\delta \mathbf{R}_{l,\gamma}$ of the position of ion γ in cell l . Following from the two methods used in the evaluation of the electron and, in particular, the phonon spectra, we have evaluated [Eq. (3)] using two distinct methods.

In our primary method, based on the VASP and PHONOPY packages, the term is approximated by identifying $U(\mathbf{r})$ with

the Hartree component of the Kohn-Sham Hamiltonian $U_H(\mathbf{r})$, and is evaluated using finite differences. Of course, the periodicity of the lattice implies that this quantity does not depend on the cell index l . We have numerically evaluated this term following Ref. [10] using VASP. In our second method, the term is evaluated entirely within the DFPT formalism using the QE and EPW packages, where $U(\mathbf{r})$ now accounts for both the Hartree and the exchange/correlation components of the potential. Once again, we have used both methods for phosphorene to verify our results, and we have found that the obtained results are in excellent agreement. Perhaps surprisingly, we must therefore conclude that our results are not very sensitive to the actual method used, provided that sufficient care is taken to use very low tolerances and fine grids in order to capture all the relevant physics.

We shall also make frequent reference to the ‘‘deformation potential’’ $DK_\eta(\mathbf{k}n, \mathbf{k}'n')$, a quantity defined implicitly by

$$\langle \mathbf{k}'n' | V_{\mathbf{q}}^{(\eta)} | \mathbf{k}n \rangle = M_{el/h-ph} = \begin{cases} n_{\mathbf{q}}^{(\eta)1/2} \\ (1 + n_{\mathbf{q}}^{(\eta)})^{1/2} \end{cases} \times DK_\eta(\mathbf{k}n, \mathbf{k}'n') \left(\frac{\hbar}{2M_{\text{cell}}\omega_{\mathbf{k}-\mathbf{k}'}}^{(\eta)} \right)^{1/2}, \quad (4)$$

having gone to infinite-area normalization, where M_{cell} is the total mass of the supercell. The scattering rate of an electron in band (or subband) n and in-plane wave vector \mathbf{k} due to a perturbation potential $V_{\mathbf{q}}^{(\eta)}$ can now be expressed as an integral only over 2D states as follows:

$$\frac{1}{\tau^{(\eta)}(\mathbf{k}, n)} = \frac{2\pi}{\hbar} \sum_{n'} \int d\mathbf{k}' |\langle \mathbf{k}'n' | V_{\mathbf{k}-\mathbf{k}'}^{(\eta)} | \mathbf{k}n \rangle|^2 \times \delta[E_n(\mathbf{k}) - E_{n'}(\mathbf{k}') \pm \hbar\omega_{\mathbf{k}-\mathbf{k}'}^{(\eta)}], \quad (5)$$

where $E_n(\mathbf{k})$ is the energy of an electron or hole with wave vector \mathbf{k} in band n .

C. Monte Carlo simulations

In order to calculate electronic transport properties employing the first-principles information we have discussed, we have followed the well-known ‘‘full-band Monte Carlo’’ method to solve numerically the Boltzmann’s transport equation for a two-dimensional electron gas. Such a method, described, for example, in Refs. [52,64,65], requires the discretization of the BZ into elements centered at points \mathbf{k}_j . The energy $E_{jn} = E_n(\mathbf{k}_j)$ and gradients $\nabla E_{jn} = \nabla_{\mathbf{k}} E_n(\mathbf{k}_j)$ for each band n are computed, stored in tables, and used to interpolate the carrier energy and group velocity. Using the Gilat-Raubenheimer algorithm [88] in two dimensions [89], the same discretization in reciprocal space is used to evaluate numerically the carrier-phonon scattering rates [Eq. (5)] as a

sum over energy-conserving mesh elements in the BZ:

$$\frac{1}{\tau^{(\eta)}(\mathbf{k}, n)} \approx \frac{2\pi}{\hbar} \sum_{jn'} \Omega_{xy} |\langle \mathbf{k}_jn' | V_{\mathbf{k}-\mathbf{k}_j}^{(\eta)} | \mathbf{k}n \rangle|^2 \times \frac{1}{(2\pi)^2} \frac{L(w_{jn'})}{|\nabla E_{jn'}|}. \quad (6)$$

where Ω_{xy} is the area in the (x, y) plane. In the notation of Eqs. (7) and (8) of Ref. [89], here $[1/(2\pi)^2] L(w_{jn})/|\nabla E_{jn}|$ is the density of states on band n in the j th element with energy $E_{jn'} = E_n(\mathbf{k}) \pm \hbar\omega_{\mathbf{k}-\mathbf{k}_j}^{(\eta)}$ and gradient $\nabla E_{jn'}$ at the center of the element \mathbf{k}_j . Details about the discretization depend on the particular crystal structure considered and will be given below. In all cases, energy conservation is numerically maintained within a root-mean-square error of less than 1 meV.

We have employed a synchronous ensemble Monte Carlo method, in light of its possible extension to the study of transients and inhomogeneous cases, although such an extension is not required here. The ensemble typically consists of 500–1000 ‘‘particles,’’ with a time step of 0.2 fs, and followed until steady state is reached in the uniform electric field we consider. Usually, steady state is only reached after several hundreds of ps at high fields, or even ns at low fields. We have also assumed a nondegenerate situation in order to avoid complications originating from Pauli’s exclusion principle. Therefore, our study is constrained to the low-density limit. Moreover, we have obtained the low-field carrier mobility using Einstein relation by calculating the diffusion constant D_θ along the direction θ , a calculation that is less affected by stochastic noise when the drift velocity is much smaller than the thermal velocity [90]. The diffusion constant is evaluated from the Monte Carlo estimator:

$$D_\theta = \frac{1}{2} \frac{d}{dt} \langle (x_\theta - \langle x_\theta \rangle)^2 \rangle, \quad (7)$$

where $\langle x_\theta \rangle$ is the time-dependent ensemble-average position along the direction θ of electrons initially at the origin $\mathbf{r} = 0$, diffusing in the absence of an electric field.

IV. ELECTRONIC TRANSPORT

The electron band structure and phonon dispersion for monolayer and bilayer phosphorene calculated using VASP and QE are shown in Fig. 4. The lattice constants obtained from the structure-relaxation procedure described above are 4.62 and 3.30 Å for monolayer and 4.51 and 3.30 Å for bilayer phosphorene, both for the VASP and QE methods and in agreement with the trend reported in Ref. [51]. For bilayers, we obtain a van der Waals gap of 3.20 Å, a value that is in excellent agreement with the value calculated by Qiao *et al.* [51]. We found empirically that a very fine mesh is necessary for the band structure to account correctly for the anisotropy and strong nonparabolicity of the electronic dispersion around the center of the BZ and in proximity of the local energy minimum along the symmetry line Q . Similarly, fine meshes are used for the deformation potentials $[DK_\eta(\mathbf{k}, \mathbf{k}')] as well, but covering the entire BZ. We should stress that initial attempts to calculate the deformation potentials over a coarser mesh have resulted in an inaccurate treatment of the scattering-angle dependence of the deformation potentials and in an overestimation of the$

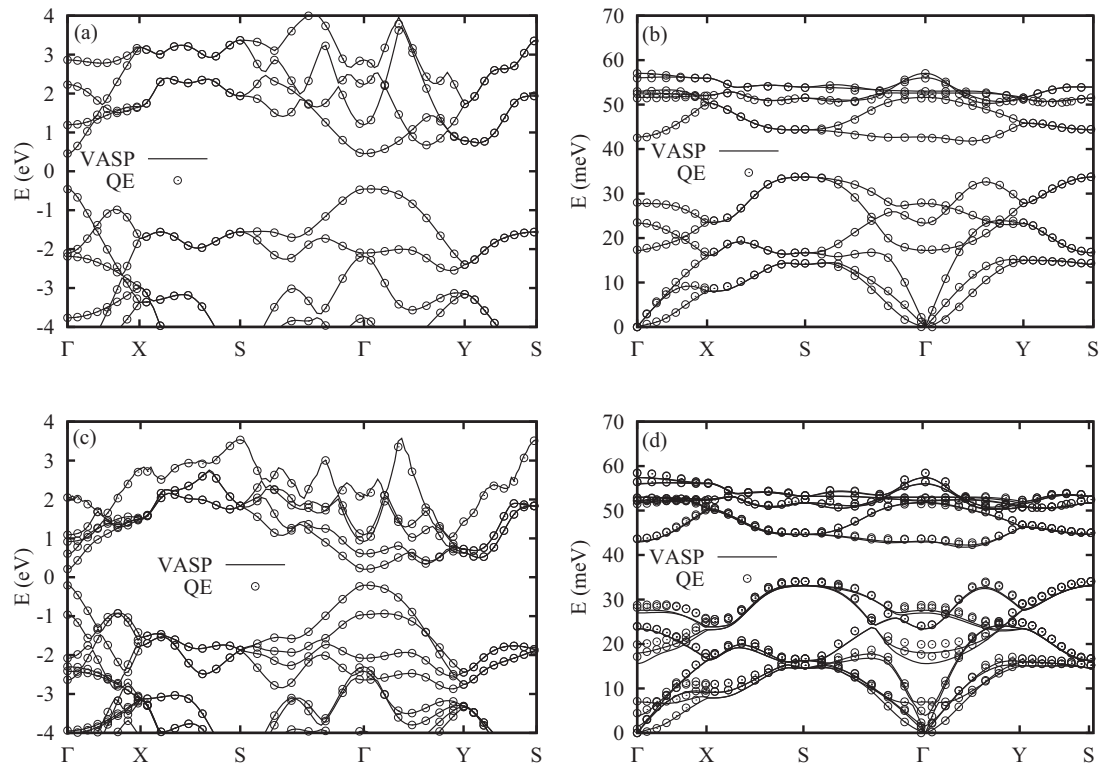


FIG. 4. The calculated band structure [left frames, (a) and (c)] and phonon dispersion [right frames, (b) and (d)], for monolayer phosphorene in (a) and (b), for bilayer phosphorene in (c) and (d).

carrier mobility. The importance of using fine mesh has also been emphasized by Ref. [78]. More details on the mesh sizes are provided in the Supplemental Material [75].

DFT calculations are known to underestimate the band gap. Indeed, the values we obtain for monolayer and bilayer phosphorene are 0.90 and 0.41 eV, lower than experimental values [51,91,92] and also smaller than the results obtained from GW calculations for monolayers, ≈ 2.0 eV (Ref. [93]). However, aside from the obvious and unavoidable impact on the effective mass, as discussed above (usually underestimated when the band gap is also underestimated), the underestimated band gaps are not expected to affect significantly the transport properties of interest since interband transitions between the valence and conduction bands are not included in our calculations.

The contour plot of energy of the first conduction band is shown in Fig. 5 only for monolayers (bilayers look qualitatively very similar). It indicates the presence of two satellite valleys, one with a minimum at the symmetry point Q and a second valley, called the Y valley minimum here, with its minimum in proximity to a point close to the Y - S symmetry line. For monolayers, the energy separation between the Γ and the Q valley minima $\Delta E_{\Gamma Q}$ is about 0.21 eV, whereas the energy separation between the Γ and the Y valley minima $\Delta E_{\Gamma Y}$ is about 0.27 eV. The electron effective masses in the nearly isotropic Q valley are 0.25 and 0.30 m_0 along the armchair and zigzag directions, respectively. For bilayers, we find similar values, both for the valley energies $\Delta E_{\Gamma Q} = 0.14$ eV and $\Delta E_{\Gamma Y} = 0.29$ eV, and for the electron effective masses in the Q valley, 0.25 and 0.32 m_0 along the armchair and zigzag directions, respectively.

Comparing the phonon spectra for monolayers, as shown in Fig. 4(b), to those calculated for bilayers in Fig. 4(d), we note the presence of low-energy optical soft modes for bilayers. The existence of such low-frequency soft modes is related to the weakness of the interlayer coupling (discussed more at length in Sec. IV C below) and also because of the heavy mass of entire unit cells in different layers oscillating out of phase in either the in-plane (LO, TO) or out-of-plane (ZO) direction. The presence of low-energy optical modes in bilayer phosphorene was also discussed recently by Xin-Hu *et al.* [94] and

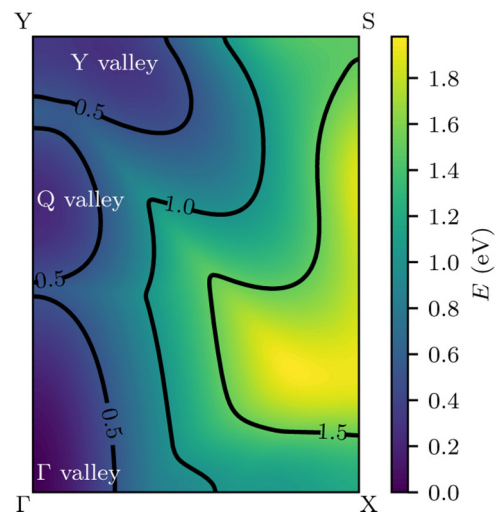


FIG. 5. Contour plot in the irreducible wedge of the Brillouin zone of the energy of the first conduction band in monolayer phosphorene.

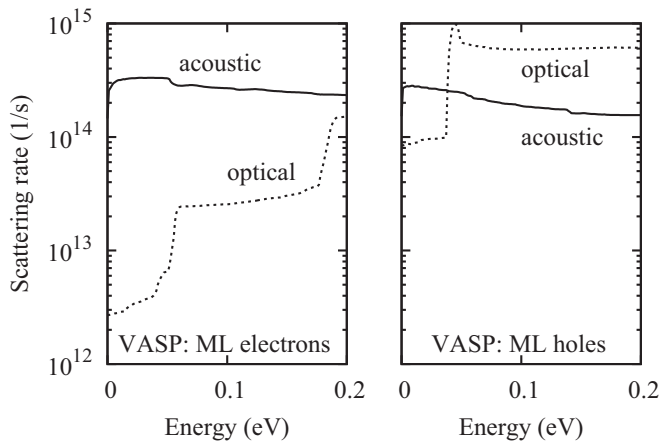


FIG. 6. Electron-phonon (left) and hole-phonon (right) scattering rates in monolayer phosphorene at 300 K where the matrix element is obtained from VASP.

has been already discussed in other multilayer systems, such as bilayer graphene [95,96]. Moreover, the coupling of these modes with electrons was also shown to be strong [96]. We shall discuss below how these modes strongly affect electronic transport in bilayer phosphorene.

A. Phosphorene monolayers

In Figs. 6 and 7, we show the angle-averaged scattering rates as a function of carrier kinetic energy obtained from VASP and QE, both for electron-phonon and hole-phonon processes. Since phosphorene is a σ_h -symmetric crystal, the ZA phonons contribution is negligible to at first order in the electron-phonon interaction [70]. Therefore, electron/ZA-phonon and hole/ZA-phonon scattering has been ignored in our transport studies. For electrons, intravalley scattering is dominated by in-plane acoustic phonons with strong backward scattering. Intervalley scattering is controlled mainly by an optical phonon (≈ 32 meV) with an intervalley deformation potential of about 1.7×10^9 eV/cm. For holes, when calculated from VASP, scattering is dominated by the intravalley ZO mode with

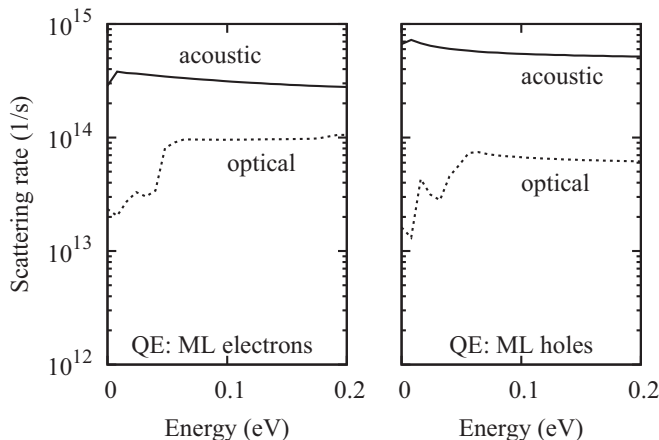


FIG. 7. Electron-phonon (left) and hole-phonon (right) scattering rates in monolayer phosphorene at 300 K. The matrix elements have been calculated using QE.

an energy of about 43 meV and a high deformation potential of 1.7×10^9 eV/cm. However, when calculated from QE, we notice that the in-plane acoustic modes dominate the scattering for holes. Comparing these results to reports in literature using similar physical models, we note that Jin *et al.* [52], using QE, have concluded that acoustic phonons are the limiting factor in the hole transport, which is consistent with our QE results. Note that this difference between VASP and QE does not translate to large differences in transport characteristics at room temperature since the 43-meV ZO mode has a low thermal population. More information, including the angular dependence of the electron/hole-phonon matrix elements, is given in Supplemental Material [75].

In Table II, we list the values for the electron and hole mobility we have obtained from the diffusion constant, both in the armchair and the zigzag directions. We obtained very similar mobilities for electrons and holes from both VASP and QE. We have already observed that our results are significantly different from those presented in Refs. [52,55] and we have speculated about possible causes for this difference. The velocity-field and energy-field characteristics for electron and hole transport are shown in Fig. 8 for a uniform electric field applied along the armchair and zigzag directions. For transport along the armchair direction, the low-field mobility obtained for electrons from the velocity-field characteristics [Fig. 8(a)] is in agreement with both the Kubo-Greenwood results presented above as well as with the value obtained from the diffusion constant. In contrast, for electron transport along the zigzag direction, the Monte Carlo simulations predict a low-field mobility a factor of ≈ 2 higher than the analytic Kubo-Greenwood estimate.

We note a rather disappointing saturated velocity of 5×10^6 cm/s for electrons, especially for a field along the zigzag direction. Interestingly, Fig. 9 shows the occurrence of significant intervalley transfer to the Q valley and even to the Y valley. However, this does not translate into any negative differential mobility since the effective masses in these satellite valleys are similar to those in the Γ valley. The hole mobility obtained from the velocity-field characteristics [Fig. 8(c)] and diffusion constant in the armchair direction is about the same as for electrons. However, the hole mobility is significantly lower along the zigzag direction due to “flatness” of the valence band along the zigzag direction. The velocity tends to deviate from linearity for electrons at very high fields. However, we do not observe any saturation even at high fields of 10^5 V/cm. At low fields, the velocities for both electrons and holes in the zigzag direction are lower than the thermal velocity, making it difficult to extract the mobility from the velocity-field characteristics numerically. Up to a field of 10^5 V/cm, the average carrier energy for electrons remains at the thermal energy (≈ 25 meV) and the electrons are in the Ohmic regime [Fig. 8(b)]. For holes, the Ohmic regime extends to even higher fields, especially in the zigzag direction [Fig. 8(d)].

B. Phosphorene bilayers

For bilayers, the angle-averaged scattering rates as a function of carrier kinetic energy obtained from VASP and QE are shown in Figs. 10 and 11. Similar to monolayers,

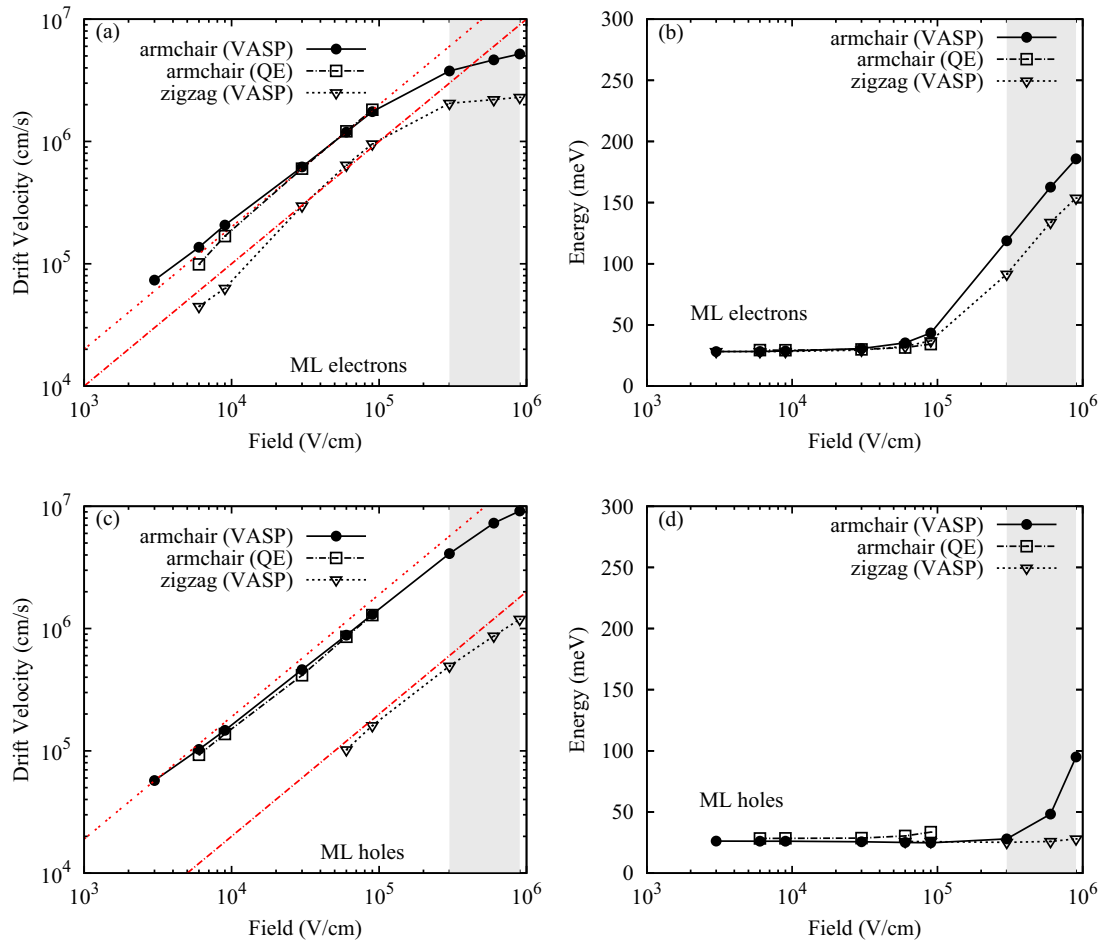


FIG. 8. (a) Drift velocity vs field (left) and (b) average energy vs field (right) characteristics at 300 K for electrons, and (c) and (d) for holes, in monolayer phosphorene calculated using full-band Monte Carlo simulations. The dashed lines in the velocity plots show the Ohmic behavior based on the mobility determined from the zero-field diffusion constant calculations. The electric field is assumed to be along the armchair or zigzag direction, as indicated. In the armchair direction, the electron-phonon matrix elements required for transport are obtained using both VASP and QE. The shaded region in the high-field regime indicates the approximate onset of scattering to higher bands, which was excluded from our model, results in this region only show a qualitative trend.

scattering with ZA phonons is ignored. For electrons, intravalley scattering is controlled to a large extent by in-plane acoustic phonons with a stronger backward scattering for the VASP

results, and in-plane acoustic modes and low-energy optical modes (1.5 and 7 meV) for the QE results. For intervalley scattering, similar to monolayers, the optical mode with an

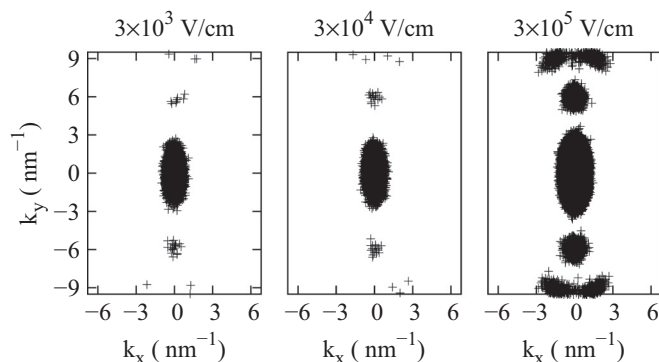


FIG. 9. Distribution in reciprocal space for electrons in monolayer phosphorene for a field of 3×10^3 (left), 3×10^4 (center), and 3×10^5 V/cm (right), along the armchair direction. Note the Γ - Q intervalley transfer at center, the Γ - Y , and Q - Y intervalley transfer at the highest field.

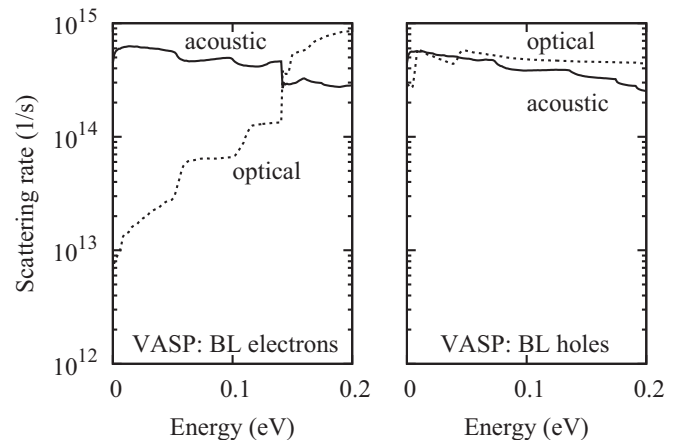


FIG. 10. Electron-phonon (left) and hole-phonon (right) scattering rates (VASP) in bilayer phosphorene at 300 K.

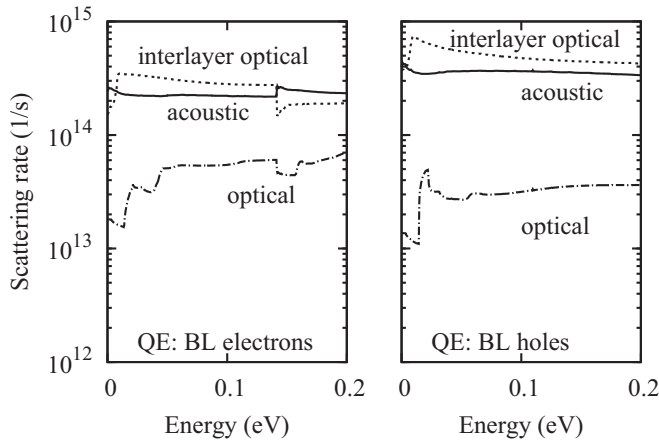


FIG. 11. Electron-phonon (left) and hole-phonon (right) scattering rates in bilayer phosphorene at 300 K. The matrix elements have been calculated using QE.

energy of 32 meV exhibits the largest deformation potential $\approx 1.7 \times 10^9$ eV/cm.

However, for holes, intravalley scattering is dominated by acoustic modes and low-energy interlayer optical modes (1.5 and 7 meV) for both VASP and QE results. More information, including the angular dependence of the electron/hole-phonon matrix elements, is given in Supplemental Material [75].

The most noticeable feature exhibited by bilayers is the presence of low-energy optical phonons. These originate from the out-of-phase oscillations of entire unit cells in the adjacent layers. Their low energy and the numerous crossing among themselves and with acoustic branches complicates the task of distinguishing these modes. This mixing may also explain the differences we have observed between results for phonon polarization vectors and carrier-phonon matrix elements obtained using VASP or QE. It is also even more important to employ a fine k -space discretization around the gamma point, observation that may explain the difference between our results and those reported in Ref. [52]. This is an important issue since these low-energy modes couple strongly with electrons and holes, as also previously observed in graphene bilayers [96]. It is exactly the presence of these modes that explains the mobility listed in Table II [obtained from the diffusion constant calculated with Monte Carlo (MC) simulations]: the carrier mobility does not increase significantly when moving from monolayers to bilayers. Actually, it may even decrease slightly, according to results obtained using VASP. As also seen in monolayers, the hole mobility in the armchair direction is about the same as for electrons, whereas in the zigzag direction, the mobility is significantly lower due to “flatness” of the valence band along the zigzag direction. The complete control of the mobility, by interlayer optical phonons, clearly assumes “free-standing” bilayers. In practice, in bilayers supported by an insulating substrate, gated, and in the presence of free carriers, dielectric screening will be very effective in suppressing the role of these modes. When ignoring their contribution, we do indeed find that both the electron and hole mobility increase by a factor of approximately 2, bringing our results close to the experimental value reported by Cao *et al.*

[31]. Finally, the velocity-field and energy-field characteristics for electron and hole transport in bilayers are shown in Fig. 12. The carrier mobility for electrons and holes obtained from velocity-field characteristics [Figs. 12(a) and 12(c)] along the armchair and zigzag directions is in good agreement with the values obtained from the diffusion constants (Table II). As also seen in monolayers, the saturated velocity for electrons in bilayers is relatively low because of the strong intervalley transfer to the Q and Y valleys. Similar to monolayers, the Ohmic regime extends up to a field of 10^5 V/cm for electrons [Fig. 12(b)] and it extends to higher fields for holes [Fig. 12(d)]. Similar to monolayers, the difference in scattering rates between VASP and QE do not translate to large differences in transport characteristics at room temperature since the total scattering rate remains essentially the same.

C. Thickness dependence of transport properties

In light of the observation we have made in the previous section regarding the low-field carrier mobility in monolayers and bilayers, it is interesting to discuss more generally the dependence of the carrier mobility on the thickness of phosphorene multilayers and bulk black phosphorus (bP).

As we have mentioned in Sec. II A, experiments show a hole mobility that is strongly dependent on thickness [28,30], with values hovering around several hundred $\text{cm}^2 \text{V}^{-1} \text{s}^{-1}$ in thick layers, sharply decreasing in layers thinner than 10 nm, being as low as $1\text{--}10 \text{ cm}^2 \text{V}^{-1} \text{s}^{-1}$ in layers 2–3 nm thin [29]. Such a behavior can be understood as the result of several effects: an increasing effective mass, a stronger carrier confinement, a larger deformation potential, and softening of the interlayer optical phonons as we move from bP to monolayers. We discuss each of these effects in turn.

1. Thickness dependence of the carrier effective mass

We have calibrated the local empirical pseudopotentials for P given in Ref. [97] to reproduce the band structure of monolayer phosphorene

$$V_P(q) = \sum_{j=1}^4 a_j e^{-b_j(q-c_j)^2} [1 - d_j e^{-f_j q^2}], \quad (8)$$

with parameters a_j , b_j , c_j , d_j , and f_j given in Ref. [97] except for $b_1 = 0.834517$ and $a_4 = 0.085232$ (in atomic and Rydberg units). The calibration has been performed using an energy cutoff of 5 Ry. The modifications of b_1 and a_4 have been made to obtain the desired band gap for monolayer phosphorene [98] (≈ 1.5 eV from Refs. [51,91,92]). The electron and hole effective masses we have obtained for bulk black phosphorus and of one-, two-, and three-layer phosphorene are shown in Tables IV and V, respectively. We have already observed that obtaining a meaningful effective mass for holes along the zigzag direction is not possible since the dispersion of the valence band along this direction (Γ - Y in few-layer phosphorene, Z - A in bulk bP) is very flat and extremely sensitive on the way the calculations are performed, as also remarked in Ref. [59]. Indeed, in some cases, the valence-band (VB) maximum is found slightly away from the Γ point [59,99–101], thus rendering the band gap of the material slightly indirect. Therefore, extracting a “curvature”

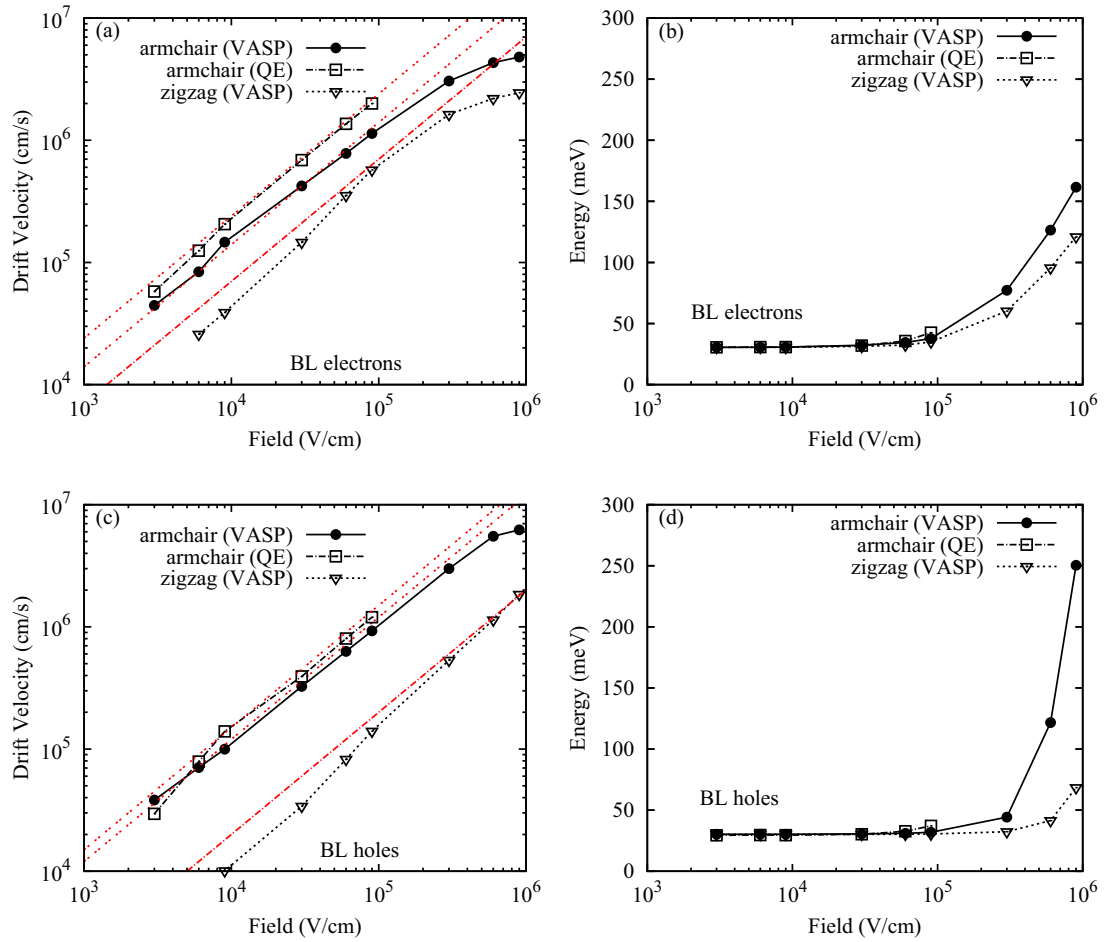


FIG. 12. (a) Drift velocity vs field (left) and (b) average energy vs field (right) characteristics at 300 K for electrons and (c) and (d) for holes, in bilayer phosphorene (VASP) calculated using full-band Monte Carlo simulations.

effective mass is impossible. In order to bypass this problem, we have calculated a conductivity mass (i.e., the slope of the dispersion) along that direction over an energy window of $k_B T \approx 25$ meV as $m_h = \hbar k_{KT} / \sqrt{50 \text{ meV}}$ where $E(k_{KT}) = 25$ meV. The thus obtained conductivity mass will give an idea about the group velocity that enters the Kubo-Greenwood formula for the mobility. (Obviously, the high density of states associated with the flat dispersion still strongly depresses the mobility via the large momentum-relaxation rates).

The results are listed in Table V. Tables IV and V also list the values of the effective masses we have obtained using

TABLE IV. Electron effective mass (in units of the free-electron mass) in phosphorene layers and bulk black phosphorus calculated using empirical pseudopotentials and DFT (in parentheses).

| | Γ -X | Γ -Y | Γ -S | DOS |
|---------------------------|-------------|-------------|-------------|------|
| Monolayer | 0.22 (0.14) | 1.1 (1.24) | 0.46 | 0.48 |
| Bilayer | 0.21 (0.10) | 1.1 (1.33) | 0.44 | 0.47 |
| Trilayer | 0.21 | 1.1 | 0.44 | 0.47 |
| | Z-Q | Z-A | Z- Γ | DOS |
| Bulk | 0.09 | 1.1 | 0.16 | 0.25 |
| Bulk (expt.) ^a | 0.0826 | 1.027 | 0.128 | |

^aExperimental data from Ref. [50].

DFT (VASP) calculations. These values are affected by a larger discretization error and are expected to be somewhat smaller compared to experimental results because of the smaller band gap predicted by DFT calculations. We see that the effective mass decreases with increasing thickness for both electrons and holes. This leads us to expect an increasing mobility when moving from monolayers to bulk black phosphorus. However, the masses decrease by an amount that is too small to explain

TABLE V. Hole effective mass (in units of the free-electron mass) in phosphorene layers and bulk black phosphorus calculated using empirical pseudopotentials and DFT (in parentheses).

| | Γ -X | Γ -Y ^a | Γ -S | DOS |
|---------------------------|-------------|--------------------------|-------------|------|
| Monolayer | 0.20 (0.14) | 1.7 | 0.59 | 0.59 |
| Bilayer | 0.19 (0.09) | 1.2 (3.08) | 0.56 | 0.51 |
| Trilayer | 0.21 | 0.91 | 0.62 | 0.49 |
| | Z-Q | Z-A | Z- Γ | DOS |
| Bulk | 0.09 | 0.51 | 0.37 | 0.26 |
| Bulk (expt.) ^b | 0.076 | 0.648 | 0.280 | |

^aOptical (slope) mass at 25 meV. The curvature mass along the Γ -Y direction cannot be defined at Γ due to the flatness of the dispersion.

^bExperimental data from Ref. [50].

the difference between bilayer and monolayer mobility behavior seen in Table I.

2. Quantum confinement effects

Intrinsically 2D materials have, among their many remarkable properties, two major advantages for the purpose of electronic devices when compared to thin “3D materials.” In thin 3D materials, quantum confinement is the result of conduction-band discontinuities with insulators (as for thin Si films confined by SiO₂ or other oxides) whereas in 2D materials, electrons are naturally confined in two dimensions by ionic potentials (as for graphene). Bulk 3D material mobilities range from respectable to excellent, but in thin films the carrier mobility is severely depressed by wave-function-overlap effects. On the other hand, 2D materials have the potential of exhibiting excellent mobilities even in the limit of atomic thickness. Moreover, confinement by insulators leads to a problematic energetic upshift of the ground-state subbands in semiconductor ultrathin films or nanowires based on 3D materials [102], causing a potentially unacceptably high gate-current leakage. Again, the naturally ionic confinement in 2D materials will save them from such an unacceptable high-gate leakage current.

Two-dimensional sp^2 (or sp^2/sp^3) group-IV materials and transition-metal dichalcogenides (TMDs) are typical examples of materials that exhibit these desired properties. In these materials, the presence of a lone electron (such as the electron occupying the p_z orbital in sp^2 group-IV materials) or the absence of unpaired electrons (such as in TMDs, with the 2–4 p electrons from the transition metal and the 6 hybrid- sp electrons from the two chalcogens) results in either a π band strongly localized in the out-of-plane direction (out of the “lone” p_z electron in the sp^2 group-IV 2D crystals), or in out-of-plane-localized states inside the 2D crystal (TMDs). In a multilayer van der Waals heterostructure, “vertical” band discontinuities at the top and bottom surfaces or interfaces, do not significantly affect the band structure. Indeed, the van der Waals coupling between adjacent layers is too small (of the order of a few tens of meV per atom both in graphene [103] and TMDs [104]) to alter the bonding properties and, most important, the out-of-plane localization of the wave functions. These materials are indeed easily exfoliated and are relatively chemically stable, a result of the out-of-plane localization of the valence-band states. Moreover, they show a very low out-of-plane conductivity, a result of the out-of-plane localization of the conduction-band states. However, the in-plane mobility remains high, even in monolayers. Indeed, graphene exhibits an extremely high mobility, $\approx 10^5$ cm² V⁻¹ s⁻¹. Such a high mobility, even for carriers confined over a thickness of the order of 0.1 nm, is the result not only of pseudospin conservation and reduced backscattering, but also of the fact that the scattering form factor of the wave functions does not depend on the confinement along the out-of-plane direction.

The recent studies by Qiao *et al.* [51] and by Xin-Hu and co-workers [94] have shown that phosphorene (and, we speculate, other group-V materials, such as also arsenene and antimonene) is remarkably different: in multilayers, the

lone p -orbital pairs hybridize into bonding and antibonding orbitals, weakly localized or even delocalized along the out-of-plane direction, with wave functions that spread across the interlayer gap. The interlayer coupling energy is now much larger: a value of 0.46 eV has been used for the interlayer coupling energy in calibrated tight-binding calculations of phosphorene [60], rendering this a “quasicovalent” bonding. This should be compared to the pure van der Waals interaction energy, of the order of a tens of meV/atom, as mentioned above. Such an effect, recently discussed at length by Xin-Hu *et al.* [94], has been shown to be responsible for the poorly understood behavior of phonon frequencies in few-layer phosphorene. These considerations imply that now the hybridized valence- and conduction-band wave functions can spread significantly across the interlayer. An additional strong hint that phosphorene multilayers are quite different from pure van der Waals materials is provided by the fact that in bulk bP, the electron mobility along the z axis (perpendicular to the plane of the layers) is about the same as along the zigzag direction: 400 cm² V⁻¹ s⁻¹ (out of plane) vs 460 cm² V⁻¹ s⁻¹ (zigzag) at 200 K, compared to 2300 cm² V⁻¹ s⁻¹ along the armchair direction [49]. The situation is similar for holes, their mobility being 540 cm² V⁻¹ s⁻¹ along the out-of-plane direction, 1300 cm² V⁻¹ s⁻¹ along the zigzag direction, and 3300 cm² V⁻¹ s⁻¹ along the armchair direction, also at 200 K (Ref. [49]). This means that carriers move from one layer to the next with relative ease. On the contrary, for graphite, the measured in-plane electron mobility is quite high, about 13 000 cm² V⁻¹ s⁻¹ at 300 K, but the material behaves essentially as an insulator along the out-of-plane direction, with a conductivity (mobility) about 3000 times lower [105,106]. This means that carriers are not transferred between layers, instead being localized within each layer.

To illustrate the non-van der Waals nature of phosphorene, in Fig. 13(a) we show the squared amplitude of the wave functions corresponding to the lowest-energy conduction-band state in bilayer phosphorene. (The van der Waals gap of 3.20 Å reported in Ref. [51] has been assumed in these empirical-pseudopotential calculations.) The wave function can be seen to “spill” into the interlayer region, for the conduction band in bilayer phosphorene. To contrast how wave functions manifest themselves in a van der Waals material, we show the conduction-band wave functions in bilayer graphene (obtained using the empirical pseudopotentials given in Ref. [65] with a van der Waals gap of 3.35 Å) in Fig. 13(b). In this case, the wave functions vanish in the interlayer region, showing that in these sp^2 layers the ionic potentials strongly confine the 2DEG within each layer.

This discussion suggests that multilayer phosphorene behaves more like a bulk covalent material than a van der Waals system, as already argued by Qiao *et al.* [51] and Xin-Hu and co-workers [94]: the “vertical” confinement of the 2DEG appears to be mainly controlled not by the ionic potentials but by the conduction-/valence-band discontinuities at top/bottom interfaces. This situation is similar to the case of semiconductor thin films or quantum wells. In such cases, carrier-phonon scattering is mainly controlled by the well-known scattering form factor [a functional of the “envelope” wave function along the out-of-plane direction z , $\zeta_n(z)$], for carriers in band

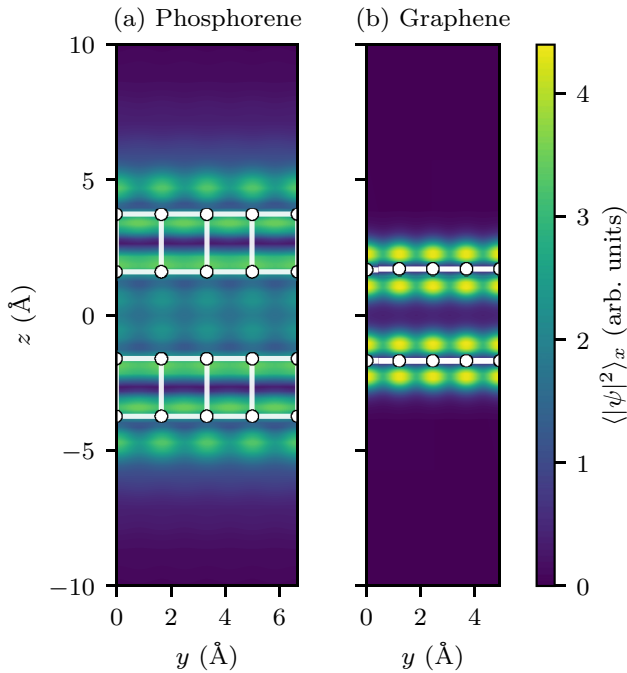


FIG. 13. (a) Squared amplitude of the wave function for the lowest-energy conduction band, averaged over a unit cell along the armchair direction for bilayer phosphorene (b) and for bilayer graphene. The atoms and bonds are indicated by balls and sticks. These results have been obtained using local empirical pseudopotentials. Note the large penetration of the conduction-band wave function into the interlayer region for bilayer phosphorene.

n , averaged over an in-plane unit cell]

$$\mathcal{I}_{nm} = \int dz |\zeta_n(z)|^2 |\zeta_m(z)|^2, \quad (9)$$

originally derived by Price [107]. This form factor increases as $1/W^2$ as the well width W (or multilayer thickness, in our case) decreases, resulting in a carrier mobility that vanishes as W^2 for small W . In a way, we are subjected to the same problems that govern Si thin-film mobility: As the thickness decreases, the mobility is depressed because of this undesired form-factor effect. In phosphorene, this may not be an effect as strong in the case of fully delocalized states, as for Si or Ge thin bodies, but it is also far removed from the more ideal cases of graphene, other group-IV monolayers, or TMDs.

Calculated form factors for the wave functions in one-, two-, three-layer phosphorene for valence-band maximum (VBM) and conduction-band minimum (CBM) are shown in Table VI. As expected, the form factor decreases with

TABLE VI. Form factor of the wave functions in monolayer, bilayer, trilayer phosphorene for the valence-band maximum (VBM) and conduction-band minimum (CBM).

| I_{mn} ($m = n$) | VBM | CBM |
|----------------------|--------|--------|
| Monolayers | 2.2417 | 1.4081 |
| Bilayers | 1.1606 | 0.7992 |
| Trilayers | 0.9463 | 0.6752 |

increasing in thickness, however, they decrease by not more than a factor of 2. Therefore, going from monolayer to bilayer phosphorene, we expect the mobility to increase by not more than a factor of 4 (the areal mass density in bilayers is twice that of monolayers). On the contrary, Cao *et al.* [31] observed an increase in mobility by a factor of 80 moving from one- to two-layer phosphorene.

3. Deformation potentials

A survey of the literature shows that the band structure changes with strain in a way that depends on the thickness of the system. In monolayers, a 4%–6% biaxial strain can have the huge effect of reversing the anisotropy [108], whereas in bulk bP strain seems to have a weaker effect [60]. This seems to suggest that the deformation potentials decrease with increasing thickness, an effect that may contribute to boosting the carrier mobility in thicker films. We have confirmed this by using the empirical pseudopotential given by Eq. (8) to calculate the change of the band gap E_G under hydrostatic stress $V_0 dE_G/dV$ (where V_0 and V are the volume of the relaxed and hydrostatically strained crystal, respectively) for monolayer phosphorene and bP. This quantity yields the sum of the conduction-band d_c and the valence-band d_v dilatation deformation potentials. For bP, using the elastic constants measured in Ref. [109] and discussed in Ref. [110], we have obtained $d_c + d_v \approx 4.3$ eV. This is about a half the value calculated in Ref. [111] and the values of 8.19–9.89 eV for $d_c + d_v$ reported in Ref. [109]. Such a discrepancy could be due to intrinsic limitations of the empirical pseudopotentials we have employed, to uncertainties in the values of the elastic constants, and to additional “internal” atomic displacements that occur under strain. On the contrary, for monolayer phosphorene, we have obtained larger dilatation deformation potentials $d_c + d_v \approx 6.6$ eV. Of course, we cannot estimate separately the contribution of the conduction band and of the valence band (given as a 33%–66% split in Ref. [112]). However, despite their uncertainty, these results constitute a highly suggestive argument to explain the larger carrier mobility in thicker films.

4. Stiffening of the interlayer optical modes

Whereas when moving from monolayers to bilayers the carrier mobility is kept low by the presence of low-energy interlayer optical modes, when moving to thicker multilayer systems this effect is expected to be less significant and even show a qualitatively opposite behavior. Indeed, the amplitude of these optical modes decreases as their energy increases. This is the result of their increased stiffness due to the coupling with various layers, as the energy of the lowest-frequency interlayer mode grows from ≈ 1.5 meV in bilayers to about 25 meV for TO phonons in bulk black phosphorus [50]. The situation is complicated by the splitting of several modes into “inner” and “surface” modes [94] in layered structures, but this trend constitutes another possible cause for a mobility increasing in thicker films.

It would be extremely interesting to study in detail the thickness dependence of all of these effects. Unfortunately, it is impossible to treat correctly the 2D-to-3D transition, and so, also the Z-to- Γ direct-band-gap transition and the

mobility change, when calculating the band structure and the vibrational properties of many-layer systems. Indeed, this would require accounting for inelastic, phase-breaking phonon scattering within a DFT (or even GW) framework, a task obviously still elusive. Yet, the results discussed here give a qualitative idea of why the carrier mobility decreases so sharply when moving from bulk black phosphorus to monolayer phosphorene. In particular, the observation that *phosphorene behaves more like a conventional semiconductor than a van der Waals material, as discussed in item 2 above, seems to explain the strong thickness dependence of the carrier mobility shown in Fig. 4(c) of Ref. [30] and suggested by Table I.*

V. CONCLUSIONS

The widely scattered theoretical predictions about the carrier mobility in 2D crystals that have been reported in the literature have prompted us to analyze critically the reasons for this confusion. Taking monolayer and bilayer phosphorene as examples of widely studied materials, we have identified the assumed simplifying isotropy of the electron-phonon matrix elements, the use of the “band” deformation potential instead of the proper carrier-phonon matrix elements, and the associated neglect of the wave-function-overlap effects as the

main sources of this confusion. Using a simple, but hopefully not oversimplified, model, we have shown that, unfortunately, the most accurate models predict the less exciting values for the carrier mobility. These do not exceed $\approx 25 \text{ cm}^2 \text{ V}^{-1} \text{ s}^{-1}$ at 300 K for both electrons and holes. We have also employed Monte Carlo simulations, based on a band structure and carrier-phonon scattering rates calculated using two separate *ab initio* DFT methods, to obtain both better estimates of the low-field mobility in phosphorene monolayers and bilayers, and information about high-field transport properties. We found that calculating the carrier-phonon interaction using small displacements and DFPT yield similar results. Our study further predicts a decrease in mobility moving from monolayers to bilayers. Most important, we have argued (unfortunately only at a qualitative level) that phosphorene, because of its lone pair of “out-of-plane” *p* electrons, behaves more like a “conventional” semiconductor than a van der Waals material, an observation that may explain the thickness dependence of the carrier mobility reported in the literature.

ACKNOWLEDGMENT

This work has been supported by Taiwan Semiconductor Manufacturing Company, Ltd. E. Chen acknowledges J. Sun for management support.

-
- [1] W. Zhang, Z. Huang, W. Zhang, and Y. Li, *Nano Res.* **7**, 1731 (2014).
 - [2] *2D Materials for Nanoelectronics*, edited by M. Houssa, A. Dimoulas, and A. Molle (CRC Press, Boca Raton, Florida, 2016).
 - [3] A. Molle, J. Goldberger, M. Houssa, Y. Xu, S.-C. Zhang, and D. Akinwande, *Nat. Mater.* **16**, 163 (2017).
 - [4] See, for example, the recent reviews of the history and state of the art of density functional theory by R. O. Jones, *Rev. Mod. Phys.* **87**, 897 (2015) or by P. J. Hasnip, K. Refson, M. I. J. Probert, J. R. Yates, S. J. Clark, and C. J. Pickard, *Philos. Trans. A: Math. Phys. Eng. Sci.* **372**, 20130270 (2014).
 - [5] G. Kresse and J. Hafner, *Phys. Rev. B* **47**, 558 (1993).
 - [6] G. Kresse, Ph.D. thesis, Technische Universität Wien, 1993.
 - [7] G. Kresse and J. Furthmüller, *Comput. Mater. Sci.* **6**, 15 (1996).
 - [8] G. Kresse and J. Furthmüller, *Phys. Rev. B* **54**, 11169 (1996).
 - [9] P. Giannozzi, S. Baroni, N. Bonini, M. Calandra, R. Car, C. Cavazzoni, D. Ceresoli, G. L. Chiarotti, M. Cococcioni, I. Dabo *et al.*, *J. Phys.: Condens. Matter* **21**, 395502 (2009).
 - [10] W. G. Vandenberghe and M. V. Fischetti, *Appl. Phys. Lett.* **106**, 013505 (2015).
 - [11] S. Baroni, S. de Gironcoli, A. Dal Corso, and P. Giannozzi, *Rev. Mod. Phys.* **73**, 515 (2001).
 - [12] F. Giustino, *Rev. Mod. Phys.* **89**, 015003 (2017).
 - [13] J. M. Ziman, *Electrons and Phonons* (Oxford University Press, Oxford, UK, 1958).
 - [14] S. Zollner, S. Gopalan, and M. Cardona, *Phys. Rev. B* **44**, 13446 (1991).
 - [15] S. Zollner, S. Gopalan, and M. Cardona, *Semicond. Sci. Technol.* **7**, B137 (1992).
 - [16] M. V. Fischetti and J. Hignman, in *Monte Carlo Device Simulation: Full Band and Beyond*, edited by K. Hess (Kluwer Academic, Norwell, MA, 1991), pp. 123–160.
 - [17] P. D. Yoder, V. D. Natoli, and R. M. Martin, *J. Appl. Phys.* **73**, 4378 (1993).
 - [18] H. J. Choi and J. Ihm, *Phys. Rev. B* **59**, 2267 (1999).
 - [19] T. Gunst, T. Markussen, K. Stokbro, and M. Brandbyge, *Phys. Rev. B* **93**, 035414 (2016).
 - [20] A. K. Geim and K. S. Novoselov, *Nat. Mater.* **6**, 183 (2007).
 - [21] M. Houssa, E. Scalise, K. Sankaran, G. Pourtois, V. V. Afanasev, and A. Stesmans, *Appl. Phys. Lett.* **98**, 223107 (2011).
 - [22] P. Vogt, P. De Padova, C. Quaresima, J. Avila, E. Frantzeskakis, M. C. Asensio, A. Resta, B. Ealet, and G. Le Lay, *Phys. Rev. Lett.* **108**, 155501 (2012).
 - [23] N. J. Roome and J. David Carey, *ACS Appl. Mater. Interfaces* **6**, 7743 (2014).
 - [24] L. Tao, E. Cinquanta, D. Chiappe, C. Grazianetti, M. Fanciulli, M. Dubey, A. Molle, and D. Akinwande, *Nat. Nanotechnol.* **10**, 227 (2015).
 - [25] X. Li, J. T. Mullen, Z. Jin, K. M. Borysenko, M. Buongiorno Nardelli, and K.-W. Kim, *Phys. Rev. B* **87**, 115418 (2013).
 - [26] M. E. Dávila, L. Xian, S. Cahangirov, A. Rubio, and G. Le Lay, *New J. Phys.* **16**, 095002 (2014).
 - [27] A. Castellanos-Gomez, L. Vicarelli, E. Prada, J. O. Island, K. L. Narasimha-Acharya, S. I. Blanter, D. J. Groenendijk, M. Buscema, G. A. Steele, J. V. Alvarez *et al.*, *2D Mater.* **1**, 025001 (2014).
 - [28] F. Xia, H. Wang, and Y. Jia, *Nat. Commun.* **5**, 4458 (2014).
 - [29] L. Li, Y. Yu, G. J. Ye, Q. Ge, X. Ou, H. Wu, D. Feng, X. H. Chen, and Y. Xiang, *Nat. Nanotechnol.* **9**, 372 (2014).

- [30] H. Liu, A. T. Neal, Z. Zhu, Z. Luo, X. Xu, D. Tománek, and P. D. Ye, *ACS Nano* **8**, 4033 (2014).
- [31] Y. Cao, A. Mishchenko, G. L. Yu, K. Khestanova, A. Rooney, E. Prestat, A. V. Kretinin, P. Blake, M. B. Shalom, G. Balakrishnan *et al.*, *Nano Lett.* **15**, 4914 (2015).
- [32] R. A. Doganov, S. P. Koenig, Y. Yeo, K. Watanabe, T. Taniguchi, and B. Öyilmaz, *Appl. Phys. Lett.* **106**, 083505 (2015).
- [33] D. Xiang, C. Han, J. Wu, S. Zhong, Y. Liu, J. Lin, X.-A. Zhang, W. P. Hu, B. Özyilmaz, A. H. Castro Neto, A. Thye, S. Wee, and W. Chen, *Nat. Commun.* **6**, 6485 (2015).
- [34] N. Gillgren, D. Wickramaratne, Y. Shi, T. Espiritu, J. Yang, J. Hu, J. Wei, X. Liu, Z. Mao, K. Watanabe *et al.*, *2D Mater.* **2**, 011001 (2015).
- [35] V. Tayari, N. Hemsworth, I. Fasih, A. Favron, E. Gaufrés, G. Gervais, R. Martel, and T. Szkopek, *Nat. Commun.* **6**, 7702 (2015).
- [36] C. Kamal and M. Ezawa, *Phys. Rev. B* **91**, 085423 (2015).
- [37] Z. Li, W. Xu, Y. Yu, H. Du, K. Zhen, J. Wang, L. Luo, H. Qiu, and X. Yang, *J. Mater. Chem. C* **4**, 362 (2016).
- [38] G. Pizzi, M. Gibertini, E. Dib, N. Marzari, G. Iannaccone, and G. Fiori, *Nat. Commun.* **7**, 12585 (2016).
- [39] Y. Xu, B. Peng, H. Zhang, H. Shao, R. Zhang, and H. Zhu, *Ann. Phys.* **529**, 1600152 (2017).
- [40] D. Singh, S. K. Gupta, Y. Sonvane, and I. Lukačević, *J. Mater. Chem. C* **4**, 6386 (2016).
- [41] J. Ji, X. Song, J. Liu, Z. Yan, C. Huo, S. Zhang, M. Su, L. Liao, W. Wang, Z. Ni, Y. Hao, and H. Zeng, *Nat. Commun.* **7**, 13352 (2016).
- [42] Y. Xu, B. Yan, H.-J. Zhang, J. Wang, G. Xu, P. Tang, W. Duan, and S.-C. Zhang, *Phys. Rev. Lett.* **111**, 136804 (2013).
- [43] F.-F. Zhu, W.-J. Chen, Y. Xu, C.-L. Gao, D.-D. Guan, C.-H. Liu, D. Qian, S. C. Zhang, and J.-F. Jia, *Nat. Mater.* **14**, 1020 (2015).
- [44] A. Suarez Negreira, W. G. Vandenberghe, and M. V. Fischetti, *Phys. Rev. B* **91**, 245103 (2015).
- [45] W. K. Ford, T. Guo, K.-J. Wan, and C. B. Duke, *Phys. Rev. B* **45**, 11896 (1992).
- [46] R. Whittle, A. Murphy, E. Dudzik, I. T. McGovern, A. Hempelmann, C. Nowak, D. R. Zah, A. Cafolla, and W. Braun, *J. Synchrotron Radiat.* **2**, 256 (1995).
- [47] D. V. Khomitsky and A. A. Chubanov, *J. Exp. Th. Phys.* **118**, 457 (2014).
- [48] F. Reis, G. Li, L. Dudy, M. Bauernfeind, S. Glass, W. Hanke, R. Thomale, J. Schäfer, and R. Claessen, *Science* **357**, 287 (2017).
- [49] Y. Akahama, A. Endo, and S. Narita, *J. Phys. Soc. Jpn.* **52**, 2148 (1983).
- [50] A. Morita, *Appl. Phys. A* **39**, 227 (1986).
- [51] J. Qiao, X. Kong, F. Yang, and W. Ji, *Nat. Commun.* **5**, 4475 (2014).
- [52] Z. Jin, J. T. Mullen, and K. W. Kim, *Appl. Phys. Lett.* **109**, 053108 (2016).
- [53] Y. Trushkov and V. Perebeinos, *Phys. Rev. B* **95**, 075436 (2017).
- [54] A. N. Rudenko, S. Brener, and M. I. Katsnelson, *Phys. Rev. Lett.* **116**, 246401 (2016).
- [55] B. Liao, J. Zhou, B. Qiu, M. S. Dresselhaus, and G. Chen, *Phys. Rev. B* **91**, 235419 (2015).
- [56] A. Al Taleb and D. Farias, *J. Phys.: Condens. Matter* **28**, 103005 (2016).
- [57] A. Balandin, *MRS Bull.* **39**, 817 (2014).
- [58] Z.-Y. Ong and M. V. Fischetti, *Phys. Rev. B* **86**, 165422 (2012); **86**, 199904(E) (2012).
- [59] L. C. Lew Yan Voon, J. Wang, Y. Zhang, and M. Willatzen, *J. Phys.: Conf. Ser.* **633**, 012042 (2015).
- [60] S. Fukuoka, T. Taen, and T. Osada, *J. Phys. Soc. Jpn.* **84**, 121004 (2015).
- [61] S. Piscanec, M. Lazzeri, F. Mauri, A. C. Ferrari, and J. Robertson, *Phys. Rev. Lett.* **93**, 185503 (2004).
- [62] M. Lazzeri and F. Mauri, *Phys. Rev. Lett.* **97**, 266407 (2006).
- [63] M. Lazzeri, C. Attaccalite, L. Wirtz, and F. Mauri, *Phys. Rev. B* **78**, 081406(R) (2008).
- [64] K. M. Borysenko, J. T. Mullen, E. A. Barry, S. Paul, Y. G. Semenov, J. M. Zavada, M. B. Nardelli, and K. W. Kim, *Phys. Rev. B* **81**, 121412(R) (2010).
- [65] M. V. Fischetti, J. Kim, S. Narayanan, Z.-Y. Ong, C. Sachs, D. K. Ferry, and S. J. Aboud, *J. Phys.: Condens. Matter* **25**, 473202 (2013).
- [66] Y. Nakamura, T. Zhao, J. Xi, W. Shi, D. Wang, and Z. Shuai, *Adv. Electron. Mater.* **3**, 1700143 (2017).
- [67] S.-I. Takagi, A. Toriumi, M. Iwase, and H. Tango, *IEEE Trans. Electron. Dev.* **41**, 2357 (1994).
- [68] Z.-G. Shao, X.-S. Ye, L. Yang, and C.-L. Wang, *J. Appl. Phys.* **114**, 093712 (2013).
- [69] X.-S. Ye, Z.-G. Shao, H. Zhao, L. Yang, and C.-L. Wang, *RCS Adv.* **4**, 21216 (2014).
- [70] M. V. Fischetti and W. G. Vandenberghe, *Phys. Rev. B* **93**, 155413 (2016).
- [71] J. Bardeen and W. Shockley, *Phys. Rev.* **80**, 72 (1950).
- [72] C. Herring and E. Vogt, *Phys. Rev.* **101**, 944 (1957); **105**, 1933(E) (1957).
- [73] M. V. Fischetti and S. E. Laux, *J. Appl. Phys.* **80**, 2234 (1996).
- [74] M. V. Fischetti and S. E. Laux, *Phys. Rev. B* **48**, 2244 (1993).
- [75] See Supplemental Material at <http://link.aps.org/supplemental/10.1103/PhysRevB.98.115416> for the description of Kubo-Greenwood method, numerical details for DFT calculations, and angular dependence plots for electron-/hole-phonon matrix elements.
- [76] J. P. Perdew and Y. Wang, *Phys. Rev. B* **45**, 13244 (1992).
- [77] J. P. Perdew, K. Burke, and M. Ernzerhof, *Phys. Rev. Lett.* **77**, 3865 (1977); **78**, 1396(E) (1996).
- [78] S. Poncé, E. R. Margine, and F. Giustino, *Phys. Rev. B* **97**, 121201(R) (2018).
- [79] P. E. Blöchl, *Phys. Rev. B* **50**, 17953 (1994).
- [80] S. Grimme, *J. Comput. Chem.* **25**, 1463 (2004).
- [81] J. Klíměš, D. R. Bowler, and A. Michaelides, *J. Phys.: Condens. Matter* **22**, 022201 (2010).
- [82] A. D. Becke, *Phys. Rev. A* **38**, 3098 (1988).
- [83] M. Dion, H. Rydberg, E. Schröder, D. C. Langreth, and B. I. Lundqvist, *Phys. Rev. Lett.* **92**, 246401 (2004).
- [84] A. Togo and I. Tanaka, *Scr. Mater.* **108**, 1 (2015).
- [85] J. Noffsinger, F. Giustino, B. D. Malone, C. H. Park, S. G. Louie, and M. L. Cohen, *Comput. Phys. Commun.* **181**, 2140 (2010).
- [86] F. Giustino, M. L. Cohen, and S. G. Louie, *Phys. Rev. B* **76**, 165108 (2007).
- [87] T. Sohler, M. Calandra, and F. Mauri, *Phys. Rev. B* **96**, 075448 (2017).

- [88] G. Gilat and L. J. Raubenheimer, *Phys. Rev.* **144**, 390 (1966); **147**, 670(E) (1966).
- [89] M. V. Fischetti, B. Fu, S. Narayanan, and J. Kim, in *Nano-Electronics Devices: Semiclassical and Quantum Transport Modeling*, edited by D. Vasileska and S. M. Goodnick (Springer, New York, 2011), pp. 183–247.
- [90] C. Jacoboni and L. Reggiani, *Rev. Mod. Phys.* **55**, 645 (1983).
- [91] V. Tran, R. Soklaski, Y. Liang, and L. Yang, *Phys. Rev. B* **89**, 235319 (2014).
- [92] S. Zhang, J. Yang, R. Xu, F. Wang, W. Li, M. Ghufran, Y. W. Zhang, Z. Yu, G. Zhang, Q. Qin, and Y. Lu, *ACS Nano* **8**, 9590 (2014).
- [93] R. Fei, A. Faghaninia, R. Soklaski, J.-A. Yan, C. Lo, and L. Yang, *Nano Lett.* **14**, 6393 (2014).
- [94] Z.-X. Hu, X. Kong, J. Qiao, B. Normanda, and W. Ji, *Nanoscale* **8**, 2740 (2016).
- [95] J.-A. Yan, W. Y. Ruan, and M. Y. Chou, *Phys. Rev. B* **77**, 125401 (2008).
- [96] C.-H. Park, F. Giustino, M. L. Cohen, and S. G. Louie, *Nano Lett.* **8**, 4229 (2008).
- [97] L. Bellaïche, S.-H. Wei, and A. Zunger, *Phys. Rev. B* **54**, 17568 (1996).
- [98] The same pseudopotential yields a band gap of ≈ 0.6 eV for bulk black phosphorus when using the same monolayer in-plane lattice constants, of ≈ 0.2 eV when using the bulk lattice constants given by Ref. [112]: $a = 3.3134$ Å, $b = 10.478$ Å, and $c = 4.3763$ Å. These values for the band gap are, respectively, larger and smaller than the experimental value (≈ 0.3 eV from Ref. [49]), presumably a result of the strong sensitivity of the calculated band gap on small variations of the lattice constants. The values for the effective mass reported in Tables IV and V for bulk bP have been obtained using the bulk lattice constants.
- [99] A. S. Rodin, A. Carvalho, and A. H. Castro Neto, *Phys. Rev. Lett.* **112**, 176801 (2014).
- [100] P. Li and I. Appelbaum, *Phys. Rev. B* **90**, 115439 (2014).
- [101] X. Peng, Q. Wei, and A. Copple, *Phys. Rev. B* **90**, 085402 (2014).
- [102] M. V. Fischetti, B. Fu, and W. G. Vandenberghe, *IEEE Trans. Electron Devices* **60**, 3862 (2013).
- [103] J.-C. Charlier, X. Gonze, and J.-P. Michenaud, *Europhys. Lett.* **28**, 403 (1994).
- [104] T. Björkman, A. Gulans, A. V. Krasheninnikov, and R. M. Nieminen, *Phys. Rev. Lett.* **108**, 235502 (2012).
- [105] H. O. Pierson, *Handbook of Carbon, Graphite, Diamond and Fullerenes-Properties, Processing and Applications* (Noyes Publications, Park Ridge, New Jersey, 1993).
- [106] M. S. Dresselhaus and G. Dresselhaus, *Adv. Phys.* **51**, 1 (2002).
- [107] P. J. Price, *Ann. Phys. (NY)* **133**, 217 (1981).
- [108] R. Fei and L. Yang, *Nano Lett.* **14**, 2884 (2014).
- [109] M. Yoshizawa, S. Endo, Y. Akahama, and S. Narita, *J. Phys. Soc. Jpn.* **55**, 1196 (1986).
- [110] S. Appalakondaiah, G. Vaitheeswaran, S. Lebègue, N. E. Christensen, and A. Svane, *Phys. Rev. B* **86**, 035105 (2012).
- [111] J. Guan, W. Song, L. Yang, and D. Tománek, *Phys. Rev. B* **94**, 045414 (2016).
- [112] H. Asahina, K. Shindo, and A. Morita, *J. Phys. Soc. Jpn.* **51**, 1193 (1982).